Tectonism and Enhanced Cryovolcanic Potential Around a Loaded Sputnik Planitia Basin, Pluto.

P. J. McGovern[1], O. L. White[2,3], and P. M. Schenk[1]

[1]Lunar and Planetary Institute, Universities Space Research Association, Houston, TX, 77058.

[2]SETI Institute, Mountain View, CA, 94043.

[3]NASA Ames Research Center, Moffett Field, CA, 94035.

Corresponding author: Patrick McGovern (mcgovern@lpi.usra.edu)

Key Points:

- The large Sputnik impact basin on Pluto is filled with nitrogen ice, producing stresses in the lithosphere that create outward-radiating fault systems.
- For likely load distributions, the pattern of faulting is strongly diagnostic of an elastic lithosphere (ice shell) thickness around 50 km.
- The initial basin depth must not have exceeded several km in order to be consistent with the observed topographic level of nitrogen ice.

Abstract

Sputnik Planitia on Pluto is a vast plain consisting of a nitrogen ice deposit filling a broad topographic depression, likely an impact basin. The basin displays a broad, raised rim and is surrounded by numerous extensional fracture systems, each with characteristic orientations with respect to the basin center. The nitrogen ice exerts a large mechanical load on the water ice outer shell crust (here also containing the lithosphere). We calculate models of stress and deformation related to this load, varying dimensional, mechanical, and boundary condition properties of the load and Pluto's lithosphere, in order to constrain the conditions that led to the formation of the observed tectonic and topographic signals. We demonstrate that the tectonic configuration is diagnostic of a particular set of conditions that hold for the Sputnik basin and Pluto, including moderate elastic lithosphere thickness (50 ± 10 km) and a wide load set into a basin that was pan-shaped and shallow (~3 km) at the time of nitrogen deposition initiation. These tectonic systems show the contributions of both flexural (bending) and membrane (stretching) responses of the lithosphere, with the latter dominating in proportion to the importance of spherical geometry effects (i.e., wide loads). Rim topography may also show an influence of primordial annular trans-basin ice shell thickening from the impact process. Analysis of stress-driven cryomagma transport shows that loading stresses can facilitate ascent of cryomagmas in annular zones around the basin, the locations of which overlap the observed distances from Sputnik of several candidate cryovolcanic sites.

Plain Language Summary

The bright Sputnik Planitia region on Pluto is a vast plain consisting of a deposit of frozen nitrogen that fills a broad depressed area. The depression is probably the result of a large object colliding with Pluto; such a depression is called an impact basin. The basin displays a broad, raised rim and is surrounded by numerous cracks that reach outward like spokes on a bicycle wheel. The frozen nitrogen pushes down the outer shell of Pluto, which consists of frozen water (ice). The pushing creates stress in the shell that can fracture it. We use computer models to test for the conditions that would create the configuration of cracks seen around Sputnik Planitia. We show that the models strongly favor a particular range for the water ice shell thickness, around 50 kilometers. Also, for the most successful models the starting shape of the depression resembled that of a frying pan, and was around 3 kilometers in depth. The models show

contributions from both bending and stretching of the shell, the latter becoming more important as the influence of the curve of Pluto's ice shell increases. The height of the basin rim may be partly a remnant of the collisional process that formed it. The stresses created in the ice shell actually assist the rising of liquid water through the water ice shell, an unusual form of volcanism that may be occuring at several sites in the region surrounding Sputnik Planitia.

1. Introduction

Following its flyby of the Pluto-Charon system in 2015, NASA's New Horizons spacecraft returned high quality images that revealed complex worlds with an unexpectedly diverse range of terrains and a correspondingly diverse range of resurfacing mechanisms, including broad tectonic systems, suggestions of cryovolcanic activity, and even ongoing surface renewal in the form of the convecting and glacially flowing nitrogen ice deposits of Sputnik Planitia on Pluto (Stern et al., 2015; Moore et al., 2016). While most of the surfaces of Pluto and Charon south of 30°S were in darkness during flyby, their "encounter hemispheres", covering roughly half of their surface areas, were resolved at 1 km/pixel or better, allowing detailed geological analyses of their surfaces to take place. The Multispectral Visible Imaging Camera (MVIC, part of the Ralph instrument) provided imaging in broadband and color channels (Reuter et al., 2008), achieving pixel scales of 315 m/pixel and 628 m/pixel for hemispheric scans on Pluto and Charon respectively, while the highest resolution imaging was obtained by the Long-Range Reconnaissance Imager (Cheng et al., 2008), achieving pixel scales of 76 m/pixel and 157 m/pixel for narrow strip mosaics on Pluto and Charon respectively. LORRI and MVIC imaging has been used to generate stereo digital terrain models (DTMs) of the encounter hemispheres of Pluto and Charon, with that for Pluto covering > 42% of its surface and varying in pixel scale from 315 m/pixel to 835 m/pixel (Schenk et al., 2018).

Pluto's encounter hemisphere is dominated by the sprawling Sputnik Planitia (hereafter abbreviated as "SP"), which forms the western portion of the heart-shaped, high albedo region of Tombaugh Regio. The Planitia is a massive deposit of nitrogen and carbon monoxide ice in solid solution (Grundy et al., 2016, hereafter referred to simply as "nitrogen ice") that partially fills a ~1300 km by ~1000 km wide depression termed the Sputnik basin; the surface of the planitia is ~3.5 km below the rim of the basin (Moore et al., 2016; Schenk et al., 2018). This basin has been interpreted as having an impact origin (Moore et al., 2016; Nimmo et al., 2016;

Johnson et al., 2016; McKinnon et al., 2016; Schenk et al., 2018), and its initial depth has been estimated to be no deeper than ~10 km based on gravity scaling the depths of basins on Iapetus (McKinnon et al., 2016). The basin is thought to be one of the oldest geologic features in Pluto's encounter hemisphere (≳4 Gyr) (Moore et al., 2016; Schenk et al., 2018), and modeling of volatile behavior in response to topography has shown that infilling of the basin with the majority of surface nitrogen ice would be complete by tens of millions of years after its formation (Bertrand and Forget, 2016; Hamilton et al., 2016; Bertrand et al., 2018), suggesting that the planitia has been a feature of Pluto's surface for much of its history. The low-viscosity nitrogen ice can be mobilized easily (Umurhan et al., 2017), and where the deposits are interpreted to be thickest towards the center of the Planitia, the cellular morphology of the plains indicate that they are undergoing solid-state convection, powered by the radiogenic heat flow emanating from Pluto's interior (Stern et al., 2015; Moore et al., 2016; McKinnon et al., 2016; Trowbridge et al., 2016). The maximum thickness of the deposits filling the basin is not known for certain, but McKinnon et al. (2016) determined that convection cell diameters of 20-40 km imply depths to the base of the nitrogen ice layer of ~3-6 km, assuming that convection is taking place in the "sluggish lid" regime. This range agrees well with the result of Mills and Montési (2019) that a minimum nitrogen ice load thickness of 4.6 km is required to explain the current topographic profile of the Sputnik basin rim as a flexural bulge forming in response to a thin elastic ice shell being loaded by the nitrogen ice.

McKinnon et al. (2017) describe the Sputnik basin rim as an eroded and modified, broad, raised ridge 250-300 km wide that rises up to ~1000 meters above the exterior plains, and argue that the elevation of the rim falls short of the ejecta thickness expected at the distance of the ridge by a factor of ~3 (cf. Melosh, 1996). They suggested that a combination of isostatic adjustment, subcrustal flow, and/or surface erosion has had the effect of lessening the ejecta blanket's topographic relief.

Reorientation of SP arising from tidal and rotational torques (Rubincam, 2003; Nimmo and Matsuyama, 2007; Keane et al., 2016) can explain the basin's present-day location, but requires the feature to be a positive gravity anomaly, despite its negative topography. The positive mass anomaly associated with the deep basin has been interpreted to be a consequence of the emplacement of several kilometers of dense nitrogen ice on a less dense cooled rigid water ice shell (1.0 g cm^{-3} and 0.917 g cm^{-3} respectively), which is similar to the emplacement of dense mare basalts for some lunar mascon basins (Melosh et al., 2013; Freed et al., 2014), as well as Pluto having a liquid water ocean, with the newly-formed basin being initially isostatically compensated by an uplift in the subsurface ocean (which also has a density of 1.0 g cm^{-3}) that caused a substantial thinning of the ice shell under the basin (Johnson et al., 2016; Keane et al., 2016; Nimmo et al., 2016). Loading of the basin with nitrogen ice would result in downward deflection of the water ice shell (Nimmo et al., 2016), and Hamilton et al. (2016) offered an alternative hypothesis to explain the basin's formation and location whereby a runaway albedo effect concentrated Pluto's nitrogen ice deposits into a single cap many kilometers thick centered near 30°N (without a pre-existing impact basin being necessary to focus them), with the resulting positive gravity anomaly subsequently locking Sputnik to a longitude directly opposite Charon. Hamilton et al. (2016) argued that the massive accumulation of nitrogen ice onto an early, thin, rigid lithosphere would have caused sufficient downward deflection of the shell to create its own basin.

The New Horizons flyby of the Pluto system did not provide any spatially resolved gravitational data and so there is no direct constraint on the compensation state of the Sputnik basin. Several groups have argued that the SP basin has been compensated to some extent (Nimmo et al., 2016; Johnson et al., 2016; Keane et al., 2016). However, Moruzzi et al. (2021) attempted to model the local gravity field over the center of the basin for a range of compensation states based on the assumption that the topography of SP follows Pluto's geoid. Their comparison of the geoid models to the topography indicate that an under-compensated basin provides the best fit, which would indicate that the Sputnik basin today is at most partially compensated by an uplifted, dense liquid ocean and is characterized by a mass deficit, although they acknowledge that the basin in the past may have been overcompensated and evolved to an under-compensated state due to refreezing of the subsurface ocean or viscous relaxation of the deeper, warmer ice. Alternatively, they found that a presently isostatically compensated basin with a thick ice shell (>300 km) also provides a good fit. Regardless of how or whether the compensation state of the Sputnik basin has changed, the loading of the basin with this kilometers-thick nitrogen ice deposit has been highly influential for Pluto's subsequent geological history, particularly in terms of governing the configuration of its tectonism.

Pluto's encounter hemisphere displays extensive tectonic deformation in the form of a non-random system of extensional faults (Keane et al., 2016), which indicates global expansion due to partial freezing of a subsurface ocean as the overarching driver of tectonism (Hammond et al., 2016; Nimmo et al., 2016). The variety of configurations and preservation states of the various fault systems suggest multiple deformation episodes and prolonged tectonic activity (Moore et al., 2016). The Sputnik basin is centered at 173°E, 25°N on the anti-Charon hemisphere, and close to the Pluto-Charon tidal axis. Keane et al. (2016) found that loading of volatile ices within a Sputnik-sized basin can substantially alter Pluto's inertia tensor, resulting in reorientation of Pluto of around 60° with respect to the rotational and tidal axes, and considered the present location of SP to be the natural consequence of the sequestration of volatile ices within the basin and the resulting reorientation (true polar wander) of Pluto. Finding that tectonism proximal to SP is oriented broadly quasi-radial to SP and that farther away (close to the edge of the encounter hemisphere) is oriented broadly azimuthally, Keane et al. (2016) argued that this orientational transition marks a change in the dominant source of stress, with loading stresses dominating near SP and reorientation stresses dominating farther away. For kilometers-thick deposits within SP, the loading stresses dominate reorientation stresses globally, and the change in stress field with time may be recorded in the crosscutting relationships of the faults, with Keane et al. (2016) predicting that the quasi-azimuthal faults far from SP may be crosscut by the quasi-radial ones closer to it.

Loading of the Sputnik basin may also have created stress conditions in the crust that are favorable for eruption of cryovolcanic material at select locations surrounding it. Tentative cryovolcanic features have been identified on Pluto (Fig. 1), the most imposing of which are Wright and Piccard Montes at the southern end of SP (Singer et al., 2016; Moore et al., 2016; Schenk et al., 2018). These features have been referred to as annular massifs, consisting of very wide and tall mounds (Wright measures 155 km across and 3.5-4.7 km high, Piccard ~240 km across and 5 km high) with enormous central depressions that can reach as deep or deeper than the edifices are tall (Schenk et al., 2018). Hekla Cavus, an oblong, flat-floored depression ~98 km in diameter and ~3 km deep located within the dark uplands of the informally named Cthulhu Macula west of SP, forms part of an ancient north-south-trending ridge-trough system (Schenk et al., 2018), and has been interpreted to have formed via collapse from subsurface deflation, possibly through cryovolcanic processes (Ahrens and Chevrier, 2021). West of Hekla, a localized zone of mantling has been identified in and around a segment of Virgil Fossae (Cruikshank et al., 2019a). Small-scale features here display muted topographic relief, and ammoniated water ice deposits have also been detected, meaning that the mantling material may be cryoclastic materials erupted by fountaining events from this segment of Virgil Fossae (Cruikshank et al., 2019a, 2019b; Dalle Ore et al., 2019). Similar cryovolcanic activity may also have occurred in Viking Terra to the north of Virgil, where a few fossae and an adjacent impact crater appear to be infilled with ammoniated, dark material, suggesting that a water-based cryolava infused with this material debouched along fault lines and flooded the fossae and crater (Cruikshank et al., 2021). Finally, smooth-textured uplands in Pioneer Terra to the northeast of SP show broad and rounded topography, and feature irregular, flat-floored depressions and scarp-bounded lowlands that reach tens of km wide and up to 3 km below the surrounding terrain, the scale of which suggests that surface collapse played a role in their formation. The depressions and smooth uplands may be intimately related, and Howard et al. (2017) hypothesized that gaseous emissions from the subsurface emanating from the depressions may have led to a methane-rich component depositing on the surrounding terrain, forming the broadly rounded divides that characterize Pioneer Terra. Cruikshank et al. (2019a) noted that the close spatial association of these various putative cryovolcanic features and SP might indicate a relationship based on enhancement of cryomagma ascent potential in an annular region beyond a large load (i.e., the nitrogen ice filling the Sputnik basin) on Pluto's water ice shell.

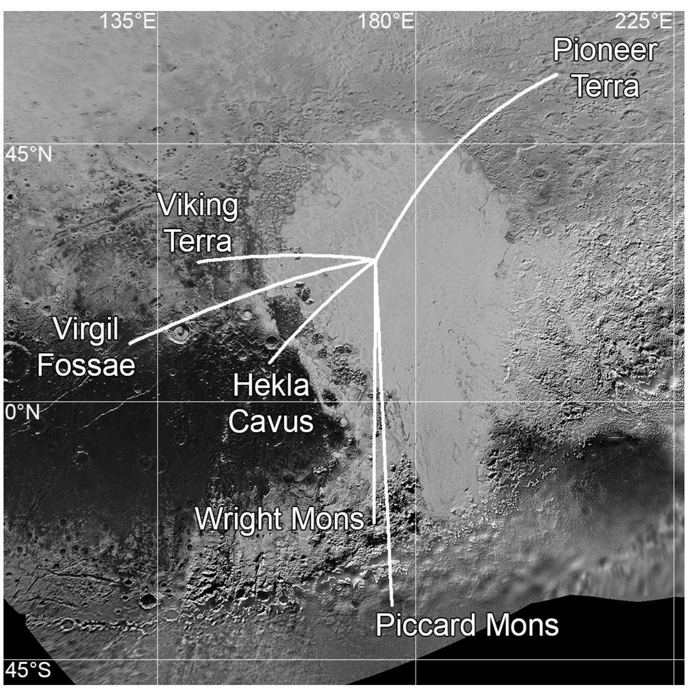

Figure 1. Locations of proposed cryovolcanic sites relative to the center of SP at 25°N, 173°E are indicated by the white lines, superimposed on a global mosaic of Pluto in equirectangular projection. Distances to each site are 527, 582, 815, 900, 957, and 1254 km for Hekla Cavus, Viking Terra, Pioneer Terra, Virgil Fossae, Wright Mons, and Piccard Mons respectively.

Here we create detailed Finite Element Method (FEM) models of impact-driven lithospheric loading on Pluto (using the COMSOL Multiphysics software package) and evaluate scenarios that are consistent with the spatial distribution and configuration of observed tectonism and proposed cryovolcanic centers.

2. Structural Mapping and Analysis

Pluto's tectonics have been surveyed previously, less than a year after the flyby (Keane et al., 2016), which was prior to the availability of the latest high quality global mosaic and DTM (Schenk et al., 2018). The datasets used for our mapping include a global mosaic that covers the encounter hemisphere at a pixel scale ranging from 234 to 835 m/pixel, and the DTM of the encounter hemisphere, which can resolve topographic features as small as ~1.5 km across and has vertical precision ranging between 90 m and 1120 m (Schenk et al., 2018). The flyby nature of the New Horizons mission meant that, for the encounter hemisphere, each point on the surface was only imaged at a single solar incidence and emission angle. Assessing topographic relief based on shading in imaging is therefore more difficult in areas around the subsolar point of 130.5°E, 51.5°N, and so the DTM plays a particularly important role in identification of fractures here, as well as in areas imaged at oblique angles near the edge of the encounter hemisphere.

Fig. 2 shows our mapping of tectonic lineations across the encounter hemisphere. We have categorized these lineations into seven distinct classes, each of which appears to bear an orientational and/or stratigraphic relationship to SP. We describe these classes below:

Ridge-Trough System: First described by Schenk et al. (2018), this is a complex, eroded, fragmentary, NNE-SSW-trending band of graben, troughs, ridges, plateaus, tilted blocks, and elongate depressions (the latter occurring within Cthulhu Macula and mapped as RTS Depressions in Fig. 2) that measures ~300 to 400 km wide and extends at least 3200 km from the north pole to the limit of coverage at ~45°S, crossing the equator at ~155°E. The structure may well extend further into the poorly resolved far side, and into the shadowed southern regions

(Schenk et al., 2018; Stern et al., 2021). The system certainly represents the earliest evidence of tectonism yet seen on Pluto due to its highly eroded state, and because its elements are invariably crosscut by other tectonic lineations. It may even predate the Sputnik basin-forming impact, but since it crosscuts the broad raised rim of the Sputnik basin and terrain leading down to SP itself, some deformation did still occur after the basin formed (Schenk et al., 2018). Equatorial crustal thickening has been hypothesized to be the cause of such an immense tectonic feature aligned along a great circle, although this would require the system to be aligned along a "paleo-equator" prior to reorientation of Pluto (McGovern et al., 2019).

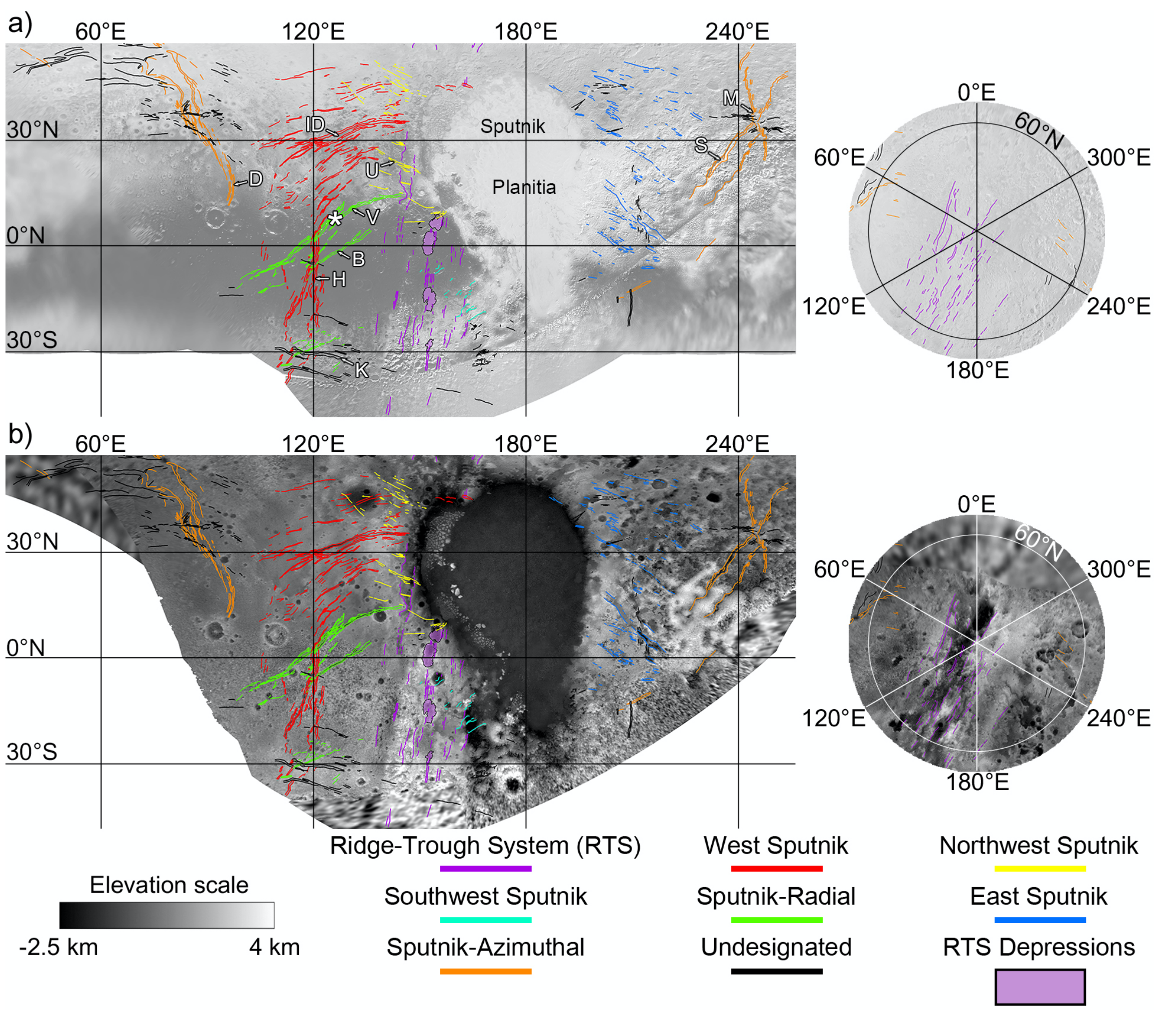

Figure 2. Mapped tectonic features across Pluto, seen in equirectangular projection south of 57°N (left), and in polar projection north of 57°N (right). The mapping is superimposed upon the global mosaic in (a) and the global DTM in (b). The colors represent the classification of the tectonics into discrete systems. Labels in (a) indicate named fossae described in the text: D = Djanggawul,

ID = Inanna and Dumuzi, U = Uncama, V = Virgil, B = Beatrice, H = Hermod, K = Kaknú, M = Mwindo, S = Sleipnir. White asterisk in (a) indicates the location of strike-slip duplexes in Virgil Fossae identified by Cruikshank et al. (2019a).

Sputnik-Azimuthal: In the far west and far east of the encounter hemisphere lie Djanggawul and Mwindo Fossae respectively, tectonic systems that are oriented circumferentially about a pole located at 170°E, 25°N, very close to the geographic center of SP, and which implies an origin tied to that feature. The fractures are removed from the pole by ~1500 and ~1100 km respectively. Mwindo Fossae are unusual in that they converge to a nexus, implying that a localized stress field caused them to diverge from the Sputnik-azimuthal orientation (McGovern et al., 2019). The geology at the nexus is unremarkable relative to its surroundings, providing no clue as to what endogenic process may have contributed to this convergence. The longest fracture of Mwindo Fossae, named Sleipnir Fossa, extends 560 km to the SW from the nexus. The modeling of Keane et al. (2016) found that reorientation of Pluto in response to infilling of the Sputnik basin with nitrogen ice would generate stresses that are approximately consistent with the Sputnik-azimuthal orientations of these systems, and that the azimuthal fractures might be crosscut by the quasi-radial ones proximal to SP (mapped as the East and West Sputnik systems in Fig. 2). We find that these azimuthal and radial systems are sufficiently removed from each other, however, such that they do not intersect, meaning that crosscutting relationships cannot be established. But the azimuthal fractures do appear older than the radial ones, in that they are more eroded and are superposed by impact craters in a few places (the radial fractures, particularly those of West Sputnik, always crosscut craters that they encounter). We note, however, that the less well-preserved appearance of the azimuthal fractures may in part be a consequence of them being located near the edge of the encounter hemisphere, where the pixel scale of New Horizons imaging is coarse (~475 m/pixel) and emission angles are high (>70°), which can make the fractures appear less sharp relative to those nearer to SP and the center of the encounter hemisphere (covered by imaging with pixel scale of ~315 m/pixel and emission angles of 30°-60°).

West Sputnik: The terrain to the west of SP (between 100°E and 150°E) displays the best-preserved tectonism in Pluto's encounter hemisphere. The West Sputnik system consists of generally sharply-defined graben and troughs, which at their northern extent are quasi-radial to SP (Inanna and Dumuzi Fossae are prominent examples of these), but which bend southwards to adopt a N-S orientation in the southern hemisphere (Hermod Fossae). Between 3°N and 5°S, these fractures intersect with the NE-SW-aligned fractures of the Sputnik-Radial system (Virgil Fossae and Beatrice Fossa). The West Sputnik fractures crosscut all craters that they encounter, indicating their relative youth. The modeling of Keane et al. (2016) indicated that these and other quasi-radial fracture systems to the east and west of SP (Sputnik-Radial, Northwest Sputnik and East Sputnik as mapped in our study) might have formed in response to loading of the Sputnik basin with nitrogen ice.

Sputnik-Radial: This fracture system consists of sharply defined graben and troughs that are similarly well preserved as those of West Sputnik, and which crosscut all craters they encounter. The main components of this system are Virgil and Beatrice Fossae which, along with a similarly oriented fracture located at 30°S 120°E, form a belt with a consistent NE-SW orientation that is essentially radial to the center of SP. At 8°N, 126°E (indicated by the white asterisk in Fig. 2a), components of Virgil Fossae form what has been interpreted to be a set of strike-slip duplexes caused by dilatational dip-slip normal faults with a right-lateral strike-slip component (Cruikshank et al, 2019a). Fractures belonging to Virgil and Beatrice Fossae appear to crosscut those of Hermod Fossae and vice-versa, suggesting that, despite their different orientations, the fractures of the West Sputnik and Sputnik-Radial systems likely formed concurrently. Ammoniated water ice deposits that appear to mantle underlying terrain have been identified in and around a segment of Virgil Fossae (Dalle Ore et al., 2019), possibly representing cryoclastic materials recently (<1 Gyr) erupted by fountaining events from this segment of the fossae (Cruikshank et al., 2019a, 2019b).

Northwest Sputnik: At its southern extent, the fractures of this system appear to be almost continuous with those of the West Sputnik and Sputnik-Radial systems. But as the Northwest Sputnik system is traced farther northwards, the divergence of the orientation of its fractures from those of West Sputnik becomes increasingly marked, such that at the northern extents of both systems their fractures are oriented at an oblique angle to one other. The convergence of all three of these quasi-Sputnik-radial systems at ~20°N 142°E may indicate that they formed during the same tectonic episode brought on by lithospheric stresses related to the formation of the Sputnik basin and its infilling with nitrogen ice (Keane et al., 2016). The Northwest Sputnik fractures are quasi-radial to SP at the southern extent of the system, becoming radial at the northern extent. They tend to be smaller scale than those of the West Sputnik and Sputnik-Radial systems, generally forming short, narrow troughs and scarps rather than wide graben hundreds of kilometers long. Where they intersect with the West Sputnik fractures, it is quite difficult to determine crosscutting relationships due to the narrowness of the Northwest Sputnik fractures: in some cases those of Northwest Sputnik seem to crosscut those of West Sputnik and vice-versa, which may be regarded as evidence for the roughly contemporaneous formation of the two systems. Cruikshank et al. (2021) identified morphological evidence of infilling of the Uncama Fossa graben (in the southern part of the Northwest Sputnik system), as well as an adjacent impact crater, with ammoniated, dark material. They suggested that the crater and fossa trough might have been recently (~1 Gyr) flooded by a cryolava debouched along fault lines in the trough and in the floor of the impact crater.

East Sputnik: Tectonism in the area to the immediate east of SP (between 185°E and 225°E) manifests as narrow scarps and troughs as well as pit chains. The alignment of the pit chains parallel to structural trends in the vicinity suggests that they are where surface collapse has occurred as tectonism disturbs an overlying mantle (Howard et al., 2017). Indeed, this region incorporates a number of terrains that are interpreted to have experienced large-scale deposition of methane-rich material since the formation of the Sputnik basin, including the bladed terrain deposits to the east (Moore et al., 2018) (and also the bright, pitted uplands separating SP from the bladed terrain, interpreted to be a modified, westerly extension of the bladed terrain deposits) and the smooth uplands to the northeast (Howard et al., 2017). The fractures of the East Sputnik system are predominantly oriented NW-SE, with those in the south being quasi-radial to SP, whereas those in the north are oriented obliquely to radial trends, and even to nearly tangential orientations near the northeast basin margin. Great circles extrapolated from the northern fractures of the East Sputnik system align fairly well with the northern fractures of the West Sputnik system, raising the possibility that these geographically separate systems may have formed as a consequence of a single tectonic episode, with lithospheric stresses being mirrored on either side of SP. Where they manifest as scarps and troughs, the East Sputnik fractures are smaller-scale than those of West Sputnik (resembling more those of Northwest Sputnik), generally have a more degraded appearance, and in a few instances are superposed by impact craters. Their degraded appearance is at least partly due to the major mantling and erosional episodes that have affected this region, which the fractures west of SP have not been subjected to. In addition, the fact that the fractures of East Sputnik often manifest as pit chains (not seen elsewhere in the encounter hemisphere) and are currently experiencing ongoing deposition of volatile ices where they occur in the bright, pitted uplands, further complicates assessment of their relative age based on preservation state.

Southwest Sputnik: This is the smallest and most tenuously defined tectonic system, which features localized clusters of NE-SW-trending ridges, scarps, and troughs on the southwestern rim of the Sputnik basin. Their sparseness lends uncertainty to the interpretation that they share an origin in a single episode of tectonism, although their quasi-radial orientation to the center of SP raises the possibility that they originated through lithospheric stresses associated with the basin.

Undesignated: All encounter hemisphere tectonics that are not classified within one of the seven aforementioned systems are termed "undesignated" for the purpose of this study. The orientation of these fractures bears no obvious stratigraphic or (quasi-)radial/azimuthal relation to the center of SP, and some may originate from localized crustal stress conditions, e.g. a cluster of reticulate networks of fractures that occur to the west of Wright and Piccard Montes, and the series of E-W-oriented fractures that form the non-Sputnik-azimuthal elements of Mwindo Fossae. Other systems, however, are regional in their extent, including a series of E-W- and WNW-ESE-trending fractures that appear to crosscut Djanggawul Fossae, and a sparsely populated belt of WNW-ESE-trending fractures (including Kaknú Fossa) that crosses Hermod Fossae at 30°S 120°E.

3. Topography of basin-filling units and surroundings

A global stereo digital elevation model (DEM) for Pluto was created from images collected by the MVIC and LORRI instruments (Schenk et al., 2018). The topographic character of both the interior of the Sputnik basin and of the terrain surrounding it is a key input to creating mechanical models of SP's loading of Pluto's icy shell lithosphere. To facilitate model generation, we take profiles across this DEM that originate from a nominal center of symmetry of SP (located at 25°N 173°E) for sectors representative of the axisymmetric nature of the northern part of SP. Profile azimuths were selected to avoid strongly non-axisymmetric influences such as the south-southeast extending embayment of SP and the ridge-trough system (purple lines in Figures 1 and 3). Individual profiles within the eastern group (Fig. 4a) show maximum relief from rim to lowest point (at the outer margin of the SP nitrogen ice deposits) approaching almost 4 km. However, the mean profile shows 3 km for this difference.

Additionally, the topography surrounding the basin is on average lower than the rim crest by about 0.8 km. We have subtracted a reference value of the far-field (radius $r > 700$ km) topography, 0.7 km elevation, from the mean profile to arrive at an average elevation of the interior nitrogen ice plains of -2 km; the plains tend to be slightly higher than this value near the basin center and lower near the margin.

The western group of profiles (Fig. 4B) shows lesser topographic variation exterior to the basin rim than those of the eastern group (Fig. 4A). We subtract the same reference far-field topography value (0.7 km) from the former as from the latter, and find an ice-margin-to-rim-peak difference approaching 3.7 km (Fig. 4B). The western mean referenced elevation profile again shows an elevation slightly higher than -2 km near the center and closer to -3 km at the margin. This transition appears to occur at a much higher value of r than for the eastern mean referenced profile, due to anomalously high elevations in the r = 300-400 km range. However, individual profiles that avoid the al-Idrisi, Zheng-He, and Baret Montes, (which are attributed to water ice blocks calving off the basin margins; White et al., 2017; O'Hara and Dombard, 2021) show a mid-basin dip below -2 km, consistent with the eastern profile. Since we consider the blocks in the various Montes to be "anomalous" and therefore not representative of the character of the general SP nitrogen ice load, we adopt a -2 km offset between the basin surface and the far-field ice shell surface in the models presented below.

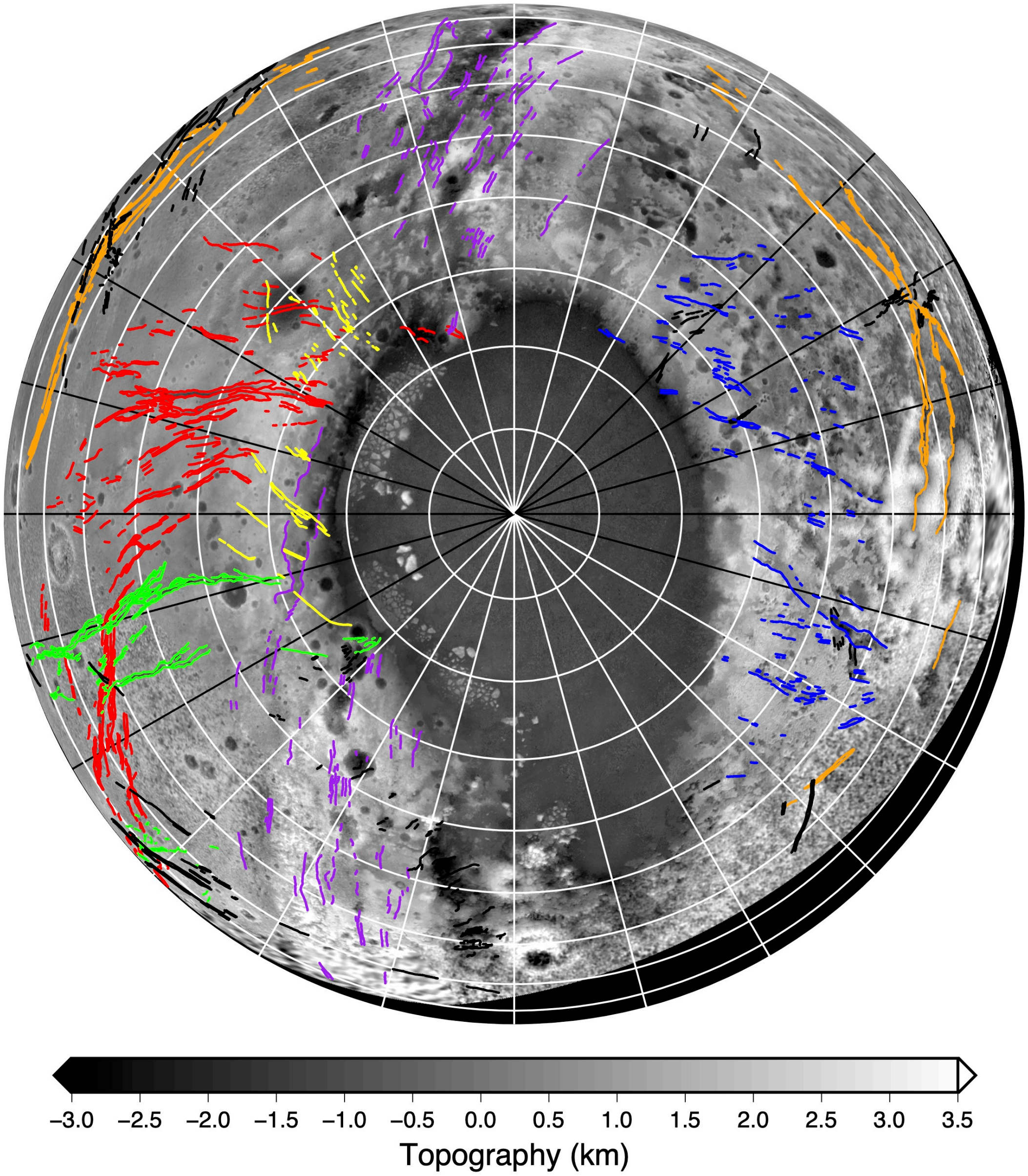

Figure 3. Hemispheric projection of circum-Sputnik Planitia hemisphere of Pluto (Orthographic projection centered on 25° N 175° E). Radial lines projected at increments of 15° in azimuth, concentric lines plotted at increments of 200 km distance from SP center. Black radial lines designate ground tracks for the east and west topographic profiles shown as dashed colored lines in Figure 4. Mapped tectonic features as in Figure 1.

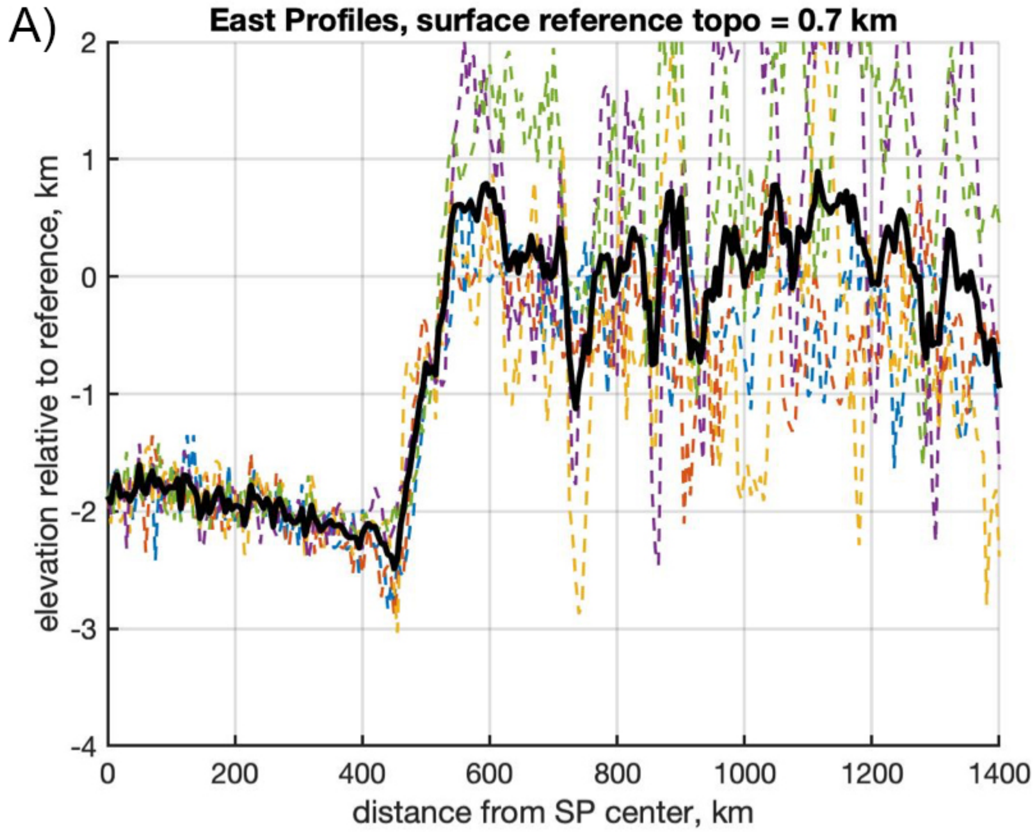
A)
East Profiles, surface reference topo = 0.7 km
elevation relative to reference, km
distance from SP center, km
2
1
0
-1
-2
-3
-4
0
200
400
600
800
1000
1200
1400

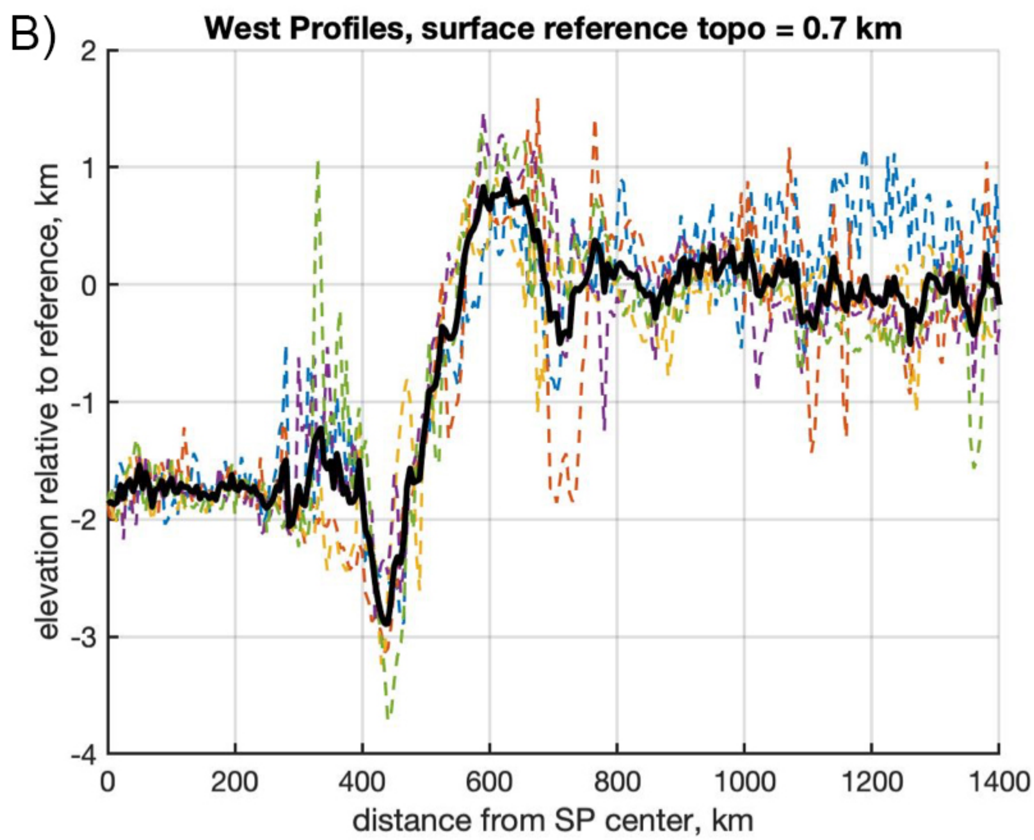
B)
West Profiles, surface reference topo = 0.7 km
elevation relative to reference, km
distance from SP center, km
2
1
0
-1
-2
-3
-4
0
200
400
600
800
1000
1200
1400

Figure 4. Selected topographic profiles (Schenk et al., 2018) for Sputnik Planitia (colored dashed lines), drawn from the geometric center of the SP basin, taken to be 25° N 175° E, sampled at 5 km increments. Horizontal axis: along-surface distance *r* from SP center. Left vertical axis: elevation above mean planetary datum; right vertical axis: local slope (degrees) calculated from adjacent points on profile. The black solid line denotes the average of the profiles. A) Eastern profiles, at azimuths of 45°, 60°, 75°, 90°, and 115°. B) Western profiles, at azimuths of 240°, 265°, 270°, 285°, and 300°. The average elevation of the terrain surrounding the basin, taken as 0.7 km for both profile groups, was subtracted from the raw topographic profiles to give relative elevation, which is the most suitable basis for comparing to the FEM models.

4. Modeling method

In order to constrain the mechanisms by which prominent tectonic systems surrounding SP have formed, we seek to explore the range of possible lithospheric responses (stress and deformation) to loads infilling the Sputnik basin. To this end, we use the COMSOL Multiphysics FEM code to calculate models of the elastic response of Pluto's icy shell lithosphere to infill of a Sputnik-sized impact basin (radius ≈ 500 km) by nitrogen ice. For computational economy, we use 2-D spherical axisymmetric geometry, with a shell encompassing the entire circumference of the planet. The nominal elastic shell (lithosphere) thickness T_e is set to 50 km, with larger and smaller values tested as well. We utilize the "free triangular" meshing scheme of COMSOL Multiphysics to create a finite element mesh within stated elastic shell boundaries (Supplementary Figures 1 and 2). The radial distance of the top surface of the shell from the origin corresponds to the radius of Pluto (R_p = 1188 km), adjusted locally to account for the preexisting basin topography (see below). The bottom surface corresponds to a radius R_p - T_e. Individual elements are constrained in size by a maximum limit T_e/20, yielding elements of order 1-2 km in size.

Note that non-elastic parts of Pluto's ice shell are not directly represented in the FEM domain. The lowermost parts of the shell are thought to be warm enough to undergo ductile deformation through creep processes in the ice [e.g., Bierson et al., 2018, 2020; Kimura and Kamata, 2020]; here it is presumed that such domains transmit the buoyant restoring forces of the ice-ocean interface to the elastic part of the shell without inducing a significant differential stress response in the ductile part. Note that the same assumption must be made any time a study of icy planet lithospheres employs purely elastic plate or shell loading solutions as part of the analysis, be it in the Pluto system [e.g., Conrad et al., 2019, 2021; Nimmo et al., 2016] or elsewhere in the solar system [e.g., Nimmo et al., 2003; Hurford et al. 2005; Giese et al., 2008; and many others].

4.1 Coordinate systems.

We use the planar axisymmetry mode of COMSOL, with distances reckoned by radius r from the symmetry axis and vertical coordinate z. However, in the study of planets there are two other useful definitions of the term "radius", requiring clarification of such terminology here. The second such definition, given above, is the radial distance from the center of the planet, defined here as the origin, also corresponding to the COMSOL origin at $(r, z) = (0, 0)$. The third is the distance from a central point to another point(s) measured along the (curved) planetary surface in map view. We plot model quantities (Figures 5-12) using this third definition, termed the "projected radial distance" r_{proj} at the model surface, itself defined by the mean radius (second definition) of Pluto at 1188 km. When we use the terms "radius" or "radial" in this paper, we are generally referring to this third definition, and we use r_{proj} in this sense. For points at the surface (e.g., the "A" components of each of Figures 5-12), this definition is straightforward. For points beneath the surface, either within the lithosphere or on the depressed central surfaces of the model impact basins, we assign r_{proj} (first definition) based on the value of r_{proj} of the point at the planetary surface that lies along the same radius line (second definition) drawn from the center of the planet. This projection from a curved to a rectilinear display (elevation vs. r_{proj}) allows for an economical display of the model results. We will define the variable z as vertical coordinate of the models, in the sense of the second definition given above; the depth below the radius of Pluto R_{p} measured along a line radiating from the planet's center.

4.2 Basin and Load dimensions.

The magnitude and shape of the infill load is constrained by topographic data for the central basin and surrounding uplands (Supplementary Figure 1) and by insights from hydrocode models of impacts into planetary bodies such as Pluto (Johnson et al., 2016) and the Moon (Potter et al., 2012; 2013, Melosh et al., 2013; Freed et al., 2014). Ultimately, it will reflect to some extent the shape of the basin at the time of initiation of infill. To represent the initial basin shape, we use a "super-Gaussian" profile of the type used to model the topography of oceanic lithospheric swells on Earth (Wessel, 1993)

$$H(r) = -d_{\mathrm{bc}} \exp((-r_{\mathrm{proj}}/w_{\mathrm{c}})^{p})$$

Where r_{proj} is projected radial distance as defined above, d_{bc} is the depth at the center of the basin (on the model symmetry axis, $r_{\mathrm{proj}} = 0$), w_{c} is a characteristic width, and p is an exponent equal to

2 for a standard Gaussian profile (in which case w_c is the half-width), with increasing values of p producing a zone of flat topography of increasing width emanating from the basin center. We assign w_c to give a basin that reaches a given r_{proj} at 1% of the central depth of the basin. As a baseline, we use a flat-bottomed basin profile with super-Gaussian exponent $p = 6$ to resemble observations of relatively "fresh" or "pristine" basins [e.g., Potter et al. 2013] and the results of hydrocode impact models [e.g. Potter et al., 2012; Johnson et al., 2016]. We also test "bowl-shaped" basins with a standard Gaussian ($p = 2$) profile and "hyper-flat" (essentially disk-shaped) basins with $p = 10$. Given the initial basin shape, we can calculate the magnitude of the initial stress state in the shell, here taken to be lithostatic: each normal stress component is set equal to $\rho_c * g * (z-H)$.

We apply nitrogen ice basin-filling loads as surface force boundary conditions, using an iterative process to determine load configurations that are consistent with observations. Successful models will produce ~ 2 km relief between the load surface and the level of the surrounding plains (Figure 4). This topography-matching requirement, in combination with the initial basin shape and shell deflection profile, will determine the ultimate thickness and shape of the load, thereby providing a constraint on nitrogen ice volumes within the basin.

The basal boundary condition at the bottom of lithosphere comprises two parts: the first is a restoring pressure proportional to the basal deflection d (sometimes called a "Winkler" foundation) of magnitude $\rho_o * g * d$, where ρ_o is the density of ocean, reflecting the buoyant support from the ocean; the second is a "counterweight" to the initial state of lithostatic stress enforced within the lithosphere (e.g., Galgana et al. 2011, 2013; Le Corvec et al., of magnitude $\rho_c * g * t_c$, where t_c is the local thickness of the shell (accounting for the initial basin topography), establishing equilibrium of the unloaded shell.

Hydrocode models of planetary basin-forming impacts also predict significant topography at the basal crustal boundary [e.g., Potter et al., 2012, 2013; Melosh et al., 2013; Johnson et al. 2016]. This topography creates post-impact lithospheric uplift that is critical to creating the gravity signature of lunar mascons [e.g., Andrews-Hanna 2013, Melosh et al. 2013; Freed et al., 2014]. To represent such effects, our models also include a "crustal collar" buoyant load at the base of the lithosphere, characterized with a simple Gaussian shape. For the nominal model we use a Gaussian half-width w_{cc} = 65 km and a load center at r_{plc} = 600 km, reflecting crustal thickening expected from the impact process. Both w_{cc} and r_{plc} are varied to test different relationships of the crustal collar to basin topography. We note that when we refer to "crustal collar" that we are referring to the subsurface structure and not any topography that the subsequent response generates, and also not to any surface topography created by ejecta.

4.3 Faulting regimes.

We characterize the faulting type predicted by the stress tensor within the shell using the $A\psi$ parameter [Simpson, 1997]. Values range over ±180°, with specific fault types corresponding to the labels above the brightest colors in Figures 5-12 at values ±150° (thrust), ±90° (strike-slip) and ±30° (normal), with the sign determining the specific orientations of the faults, as labeled in the figures. Values in-between these represent mixed modes of faulting. Values of ±180° correspond to compression with ambiguous orientation (termed "pure constriction"), and similarly for value of 0° for extension ("pure extension"). We will identify the presence of a specific fault type plus orientation prediction as a stress "regime" (e.g., radial normal regime zone) rather than say "radial normal fault zone", because faulting per se is not predicted to happen where the failure criterion is not satisfied.

4.4 Material Properties and Failure Criterion.

We adopt material properties appropriate to the water ice and nitrogen ice constituents of the models (Table 1). We recognize that strength-type properties of deformed large-scale rock (ice) assemblages often fall short of laboratory derived values. Following this philosophy, we adopt a Young's Modulus value for water ice of 5 MPa, intermediate between values of order 1 MPa from field observations (e.g., Vaughan et al., 1995) and 9 MPa from laboratory-scale specimens (e.g., Petrenko and Whitworth, 1999); See also the discussion in Nimmo (2004). We construct Mohr-Coulomb failure envelopes with parameters cohesion c = 1 MPa and angle of internal friction angle $\phi = 30°$.

4.5 Stress definitions.

We adopt an axisymmetric spherical shell system with three primary normal stress components. The locally horizontal components are σ_h and σ_ϕ, in the plane of the model and perpendicular to it, respectively; σ_ϕ is sometimes called the "hoop stress". The vertical component (i.e., pointing to the central point contained within the shell) is called σ_v. We also define a "tectonic stress" after Rubin [1995] for each horizontal component: $\sigma_{Th} = \sigma_h - \sigma_v$. and $\sigma_{T\phi} = \sigma_\phi - \sigma_v$. These components are useful to characterize the tectonic implications of specific stress tensor configurations and for calculating cryomagma ascent criteria within dikes. We use the "engineering" convention that tension is positive and compression is negative in sign.

4.6 Cryomagma ascent criteria.

Following McGovern et al. (2013, 2016), we use 2 criteria for cryomagma ascent: 1) The stress orientation criterion requires that the least compressive stress be oriented horizontally to allow vertical dikes to form (e.g., Anderson, 1953). This criterion can be expressed as $\sigma_T > 0$, for either of the tectonic stress components. 2) We use the formulation of Rubin (1995) to calculate cryomagma ascent velocity u_z within vertical dikes, using the vertical gradients of tectonic stress components $d\Delta\sigma_T/dz$,

$$u_z = (1/3\eta)\, w^2\, (d\Delta\sigma_T/dz + \Delta\rho g + d\Delta P/dz) \qquad (1)$$

where η is (cryo)magma viscosity, w is dike width, $\Delta\rho$ is density contrast between magma and host rock (here, between liquid water and the water ice shell), g is planetary gravity, and ΔP is magma overpressure. The first and second terms on the right hand side of eqn. (1) can be equated to yield a solution for an effective buoyant density $\Delta\rho_{efb}$ that can offset negative buoyancy of water in ice (here taken to be -80 kg/m^3).

5 Modeling Results

We first describe the stress state and deformation (Fig. 5) induced by a baseline ("nominal") model with an initial "pan-shaped" (McGovern, 2001) basin with d_{bc} = 3 km, p = 6, and r_{proj} = 500 km (yielding w_c = 387.6 km). Near the symmetry axis, the applied basin-filling load produces horizontal stress components σ_h and σ_ϕ that are compressional throughout almost the entire thickness of the lithosphere. At the surface of the lithosphere, the magnitudes of these stresses (red and black lines in Fig. 5a, respectively) are nearly identical (with $|\sigma_\phi|$ slightly higher in mid-basin), resulting in a fault regime prediction of generic compression ("pure constriction", light purple colors in Figure 5), although any such faults would be obscured by the nitrogen ice load. In the outer region of the basin (380 km < r_{proj} < 4300 km), with increasing radial distance r_{proj}, the stress regimes cycle through narrow zones of radial thrust, strike-slip, and concentric normal, ultimately reaching a wider region characterized by the radial normal regime out to 640 km, as σ_h and σ_ϕ diverge in magnitude. Further outward, a strike-slip regime extends to well beyond r_{proj} = 1000 km.

The failure criterion is exceeded in two surface regions: a region beneath the load ($0 < r_{proj} < 270$ km) characterized by pure constriction, and a broader zone beyond the load ($450 < r_{proj} < 850$ km) that comprises proximal radial normal faulting and distal strike-slip faulting (Fig. 5b). For $r_{proj} > 640$ km, a strike-slip regime is seen at the bottom and through most of the depth of the lithosphere, and for $r_{proj} > 650$ km the entire lithosphere is in strike-slip mode (Fig. 5). These findings stem from the extensional out-of-plane stress σ_ϕ produced by the membrane response of a curved (spherical) lithosphere (Turcotte et al., 1981) The effective buoyant density calculated from the vertical gradient of the out-of-plane tectonic stress $\Delta\rho_{efb}$ is elevated, with peak values of about 60 kg/m^3, in a region $450 < r_{proj} < 650$ km, providing a partial offset of the negative buoyancy of water in ice. This offset appears strongest at the bottom of the lithosphere. This region also satisfies the stress orientation criterion ($\sigma_\phi > 0$) throughout its radial width, owing to the extensional membrane contribution to the out-of-plane stress σ_ϕ throughout the thickness of the lithosphere (see sub-section "*Interplay of flexural and membrane support*" in the Discussion).

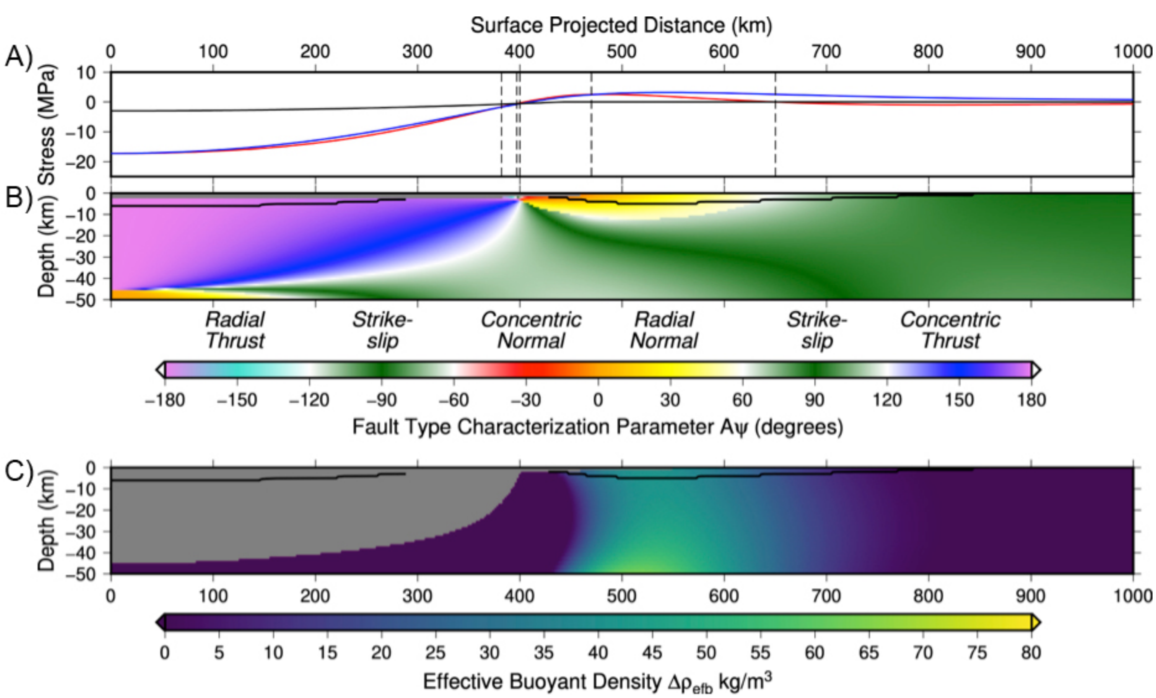

Figure 5. State of stress in an FEM model of Pluto's icy shell lithosphere, subject to loading by nitrogen ice infill of a Sputnik Planitia-sized basin. The shell model domain is shown as a rectilinear projection model (after Freed et al., 2001) where horizontal coordinate r_{proj} corresponds to distance from the symmetry axis along the surface of the spherical shell. This is the nominal model with elastic shell thickness $T_e = 50$ km. (A) Normal stress tensor components σ_ϕ (out of

plane, black curve), σ_h (horizontal in-plane, red curve), and σ_v (vertical, blue curve) at the surface (z = 0) are functions of radius r_{proj} from model center. Vertical dashed lines delineate major crossovers in normal stress magnitudes, corresponding to boundaries of predicted fault regimes in (B). (B) Cross-section map of the parameter $A\psi$ (Simpson et al., 1997), delineating "fault type regimes". Color scale at bottom after Freed et al. (2001), modified to give transitional colors between the regimes. "Pure" fault regime labels (corresponding to values of ± 30°, 90°, and 150°) are given atop color scale. Solid black contours bound regions where a Mohr-Coulomb failure criterion is satisfied. (C) Effective buoyant density $\Delta\rho_{efb}$ calculated from vertical gradient of the out-of-plane tectonic stress. Solid black contours as in (B). Regions for which σ_ϕ is not the most extensional stress (i.e., where the stress orientation criterion for radial diking is not met) are masked out by grey.

Adding a subsurface buoyant load ("crustal collar") reflecting the post-impact configuration of the shell can significantly change the shell stress state, with important implications for stress regimes, observed faulting, and cryomagma ascent potential (Fig. 5). For a model with crustal collar characteristic width 65 km and center projected distance 650 km (Fig. 6), the lateral and vertical extents of the radial normal regime zone are larger relative to the nominal case in Fig. 5, as are those of the region that satisfies the failure criterion. Thus, the addition of the crustal collar load significantly enhances the potential for normal faulting oriented radially to Sputnik basin, although we note that the $A\psi$ parameter moves close to pure extension near the center of the zone. The effective buoyant density calculated from the vertical gradient of the out-of-plane tectonic stress shows a region ranging from ≈ 580-720 km where $\Delta\rho_{efb}$ is greater than 80 kg/m^3, thereby allowing cryomagma ascent despite the negative buoyancy of water in ice. This region also satisfies the stress orientation criterion (σ_ϕ > 0) throughout its entirety, again owing to the extensional membrane component of stress.

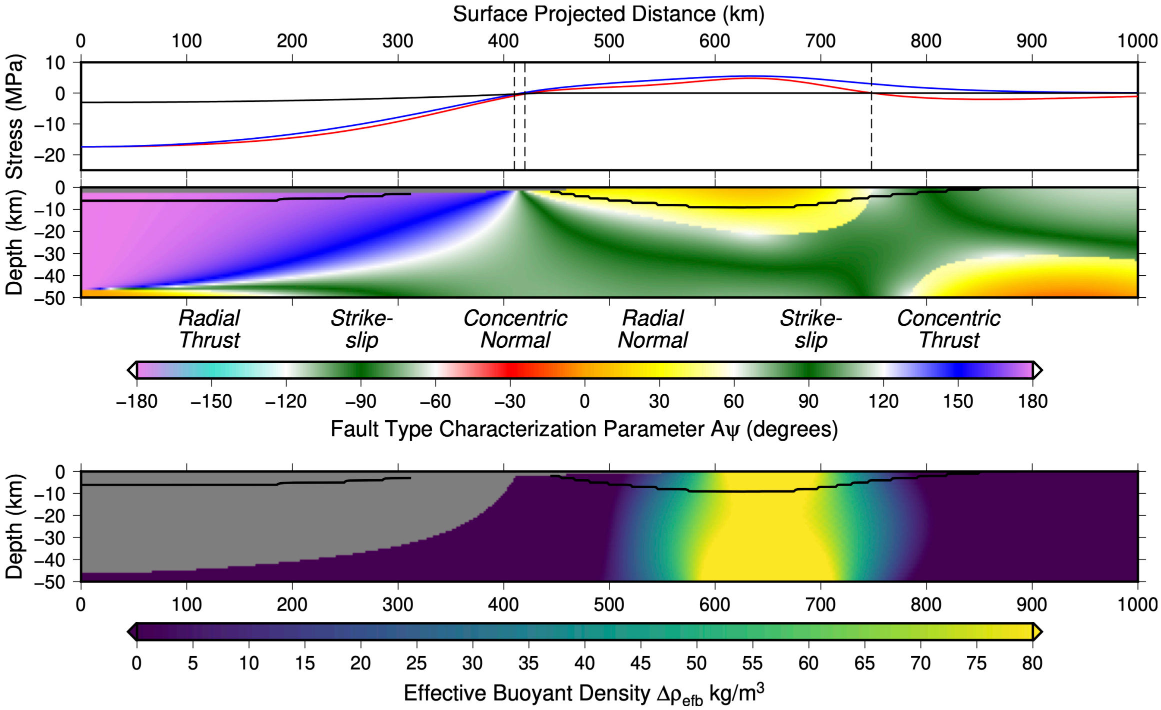

Figure 6. As in Figure 5, for case with a crustal collar buoyant load, as specified in the text.

Lithospheric thickness plays a key role in modulating the stress response to loads. For a model with shell thickness T_e = 30 km (Fig 7), the configuration of stress is markedly different from the nominal case, with a large separation of the horizontal normal stress magnitudes at the surface (Fig. 7a) and a prediction of strike-slip regime throughout almost the entire lithosphere beyond the basin. Only a tiny excursion of σ_h above the vertical normal stress (= 0 beyond the load) at the surface for r_{proj} between ~ 420 and 540 km produces a narrow and extremely shallow zone of radial normal regime. The depths of predicted failure regions beneath the load and beyond it are both substantially deeper and broader than for the nominal case (Figure 5), nearly penetrating the entire thickness of the shell (Figure 7b). This condition reflects the greatly elevated stress magnitudes resulting from the greater load magnitude, as required to meet the topographic constraint on the weaker lithosphere, see Figure 13). Cryomagma ascent is greatly enhanced in an annular zone 450 km < r_{proj} < 600 km, with $\Delta\rho_{efb}$ values well in excess of 80 kg/m^3.

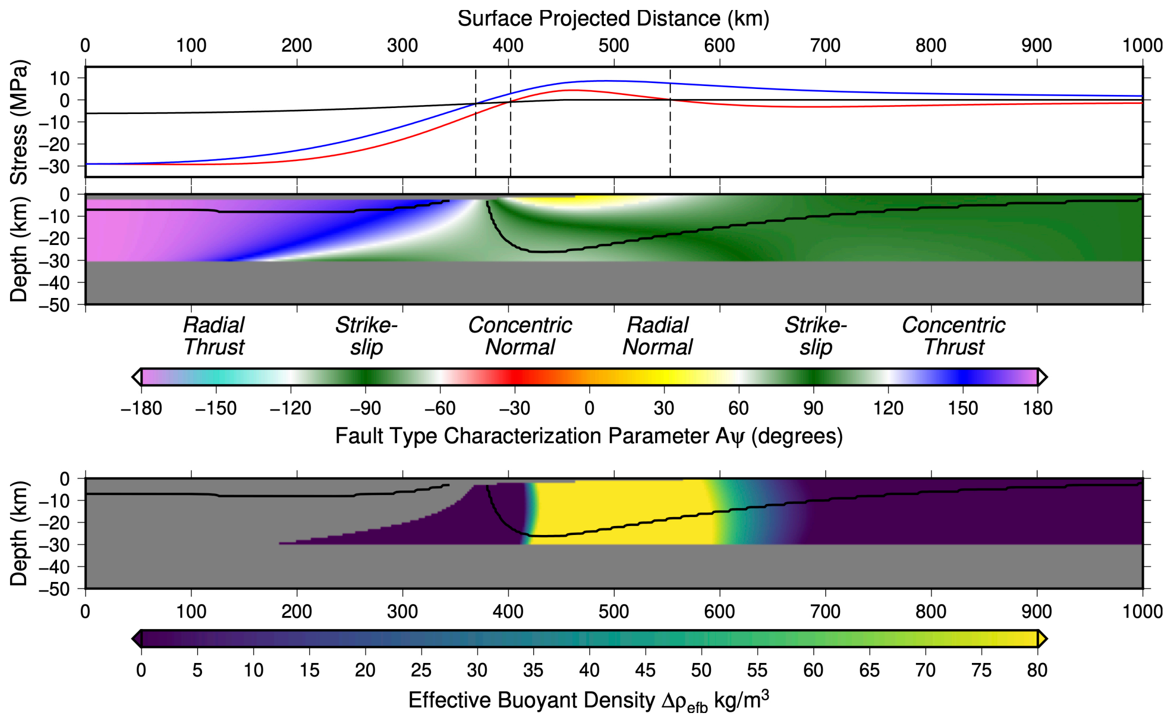

Figure 7. As in Figure 5, for T_e = 30 km. Note greater range on stress scale relative to previous Figures.

For a T_e = 30 km case with a crustal collar model (Fig. 8), the stress regime is broadly similar to the model without the collar, but with the diminishment of the small radial normal regime zone near the basin margin and the creation of a larger radial normal regime zone above the collar load ($580 < r_{proj} < 710$ km). Similarly, the zone of enhanced $\Delta\rho_{efb}$ moves outwards in r_{proj} to reside above the collar load.

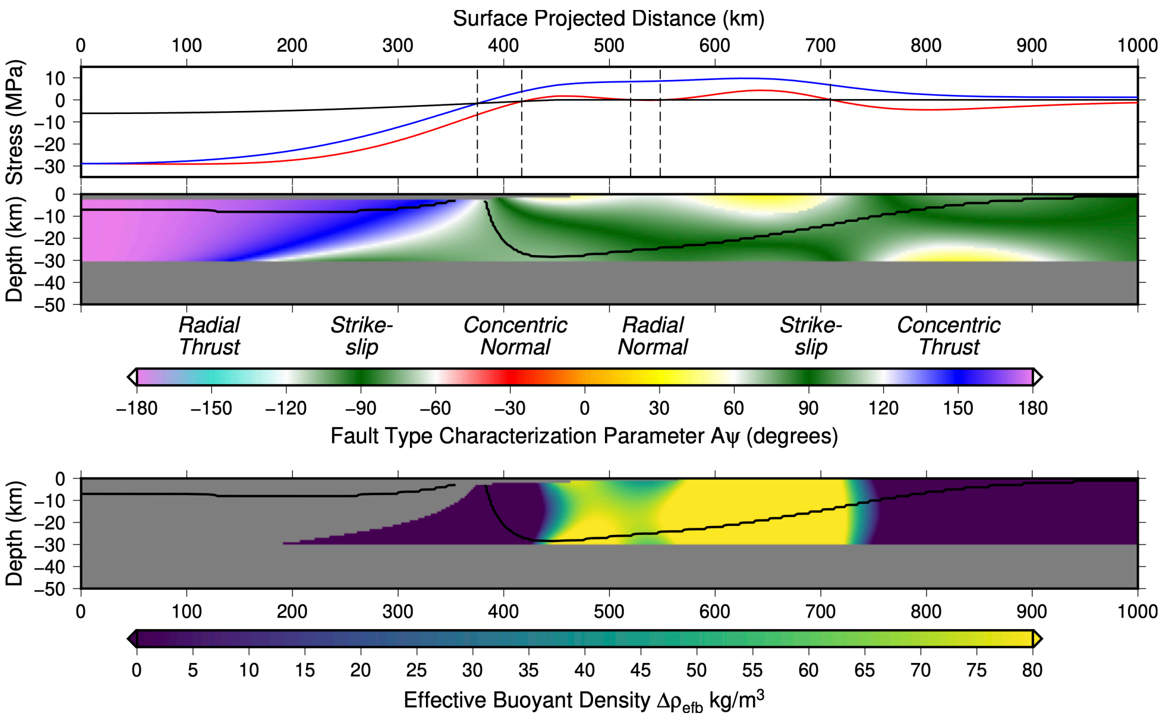

Figure 8. As in Figure 7, for case with a crustal collar buoyant load.

A model with T_e = 70 km (Fig. 9) shows substantial differences from the previous two cases, but also some similarities. As with the T_e = 50 km case (Fig. 5), when T_e = 70 km the horizontal stresses at the surface of the shell are similar in magnitude to each other (although somewhat lower than their equivalents when T_e = 50 km). However, the surface stress regimes at the outer part of the basin for T_e = 70 km go through a cycle of radial thrust, strike slip, concentric normal, and radial normal between 360 and 730 km, with only the latter 2 potentially visible beyond the edge of the load (r_{proj} ~ 450 km). The zones of predicted failure are markedly narrower in r_{proj} and shallower in depth than for the T_e = 50 km case, with the normal fault zone being barely 80 km in extent and entirely concentric in character. Peak $\Delta\rho_{efb}$ values of about 15-20 kg/m^3 are also much smaller than for the T_e = 50 km case. The latter properties of this model reflect the much thinner load compared to the models with thinner shells, again dictated by the topography constraint (Fig. 13).

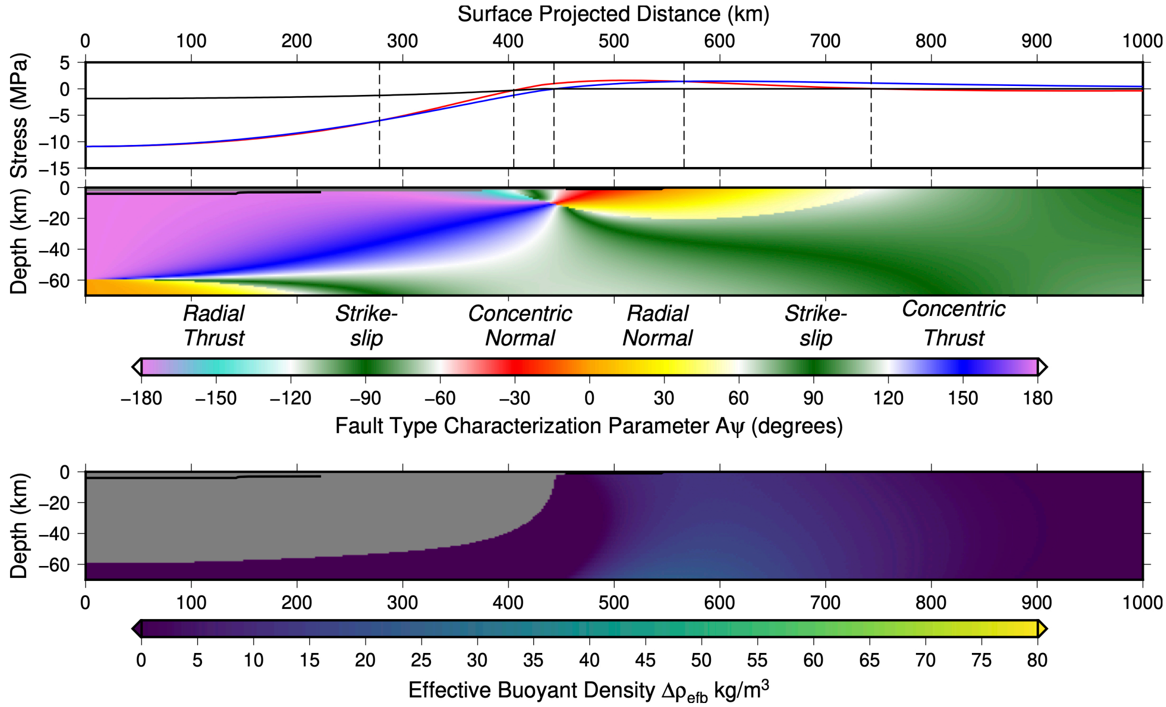

Figure 9. As in Figure 5, for T_e = 70 km . Note that the stress and depth vertical axes have lesser and greater ranges, respectively, than for previous figures.

A model with T_e = 70 km and a crustal collar load (Fig. 10) shows a shrinking of the surface strike-slip regime zone and a significant expansion of extent and depth of the zone containing the two normal fault regimes. Of these, the concentric normal regime zone covers most of the surface (440 km < r_{proj} < 690 km), although the most distal part of this combined zone, and most of its depth, fall into the radial normal regime Values of $\Delta\rho_{efb}$ approach 50 kg/m^3 above the crustal collar (Fig. 10c), comparable to those observed in the T_e = 50 km model without the collar load (Fig. 5c).

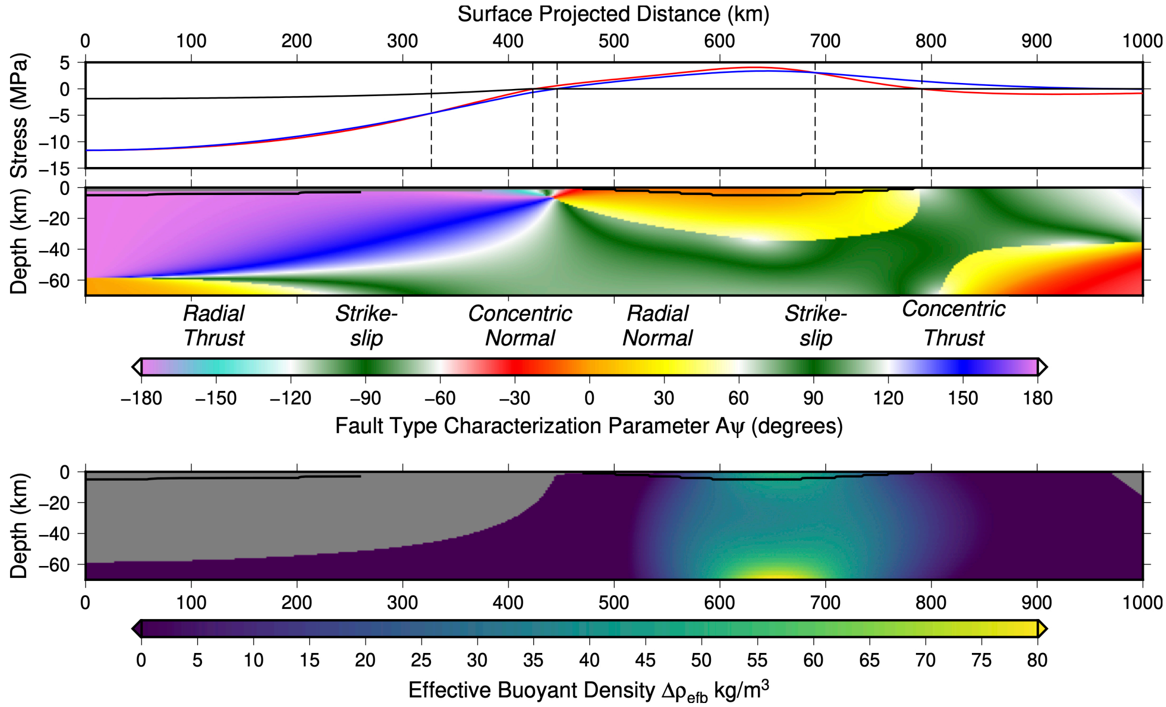

Figure 10. As in Figure 9, for case with a crustal collar buoyant load.

To investigate the effects of potential variations in the pre-loading central (maximum) depth of the basin d_{bc}, we calculated pan-shaped basin models with d_{bc} = 4, 5, and 6 km (and otherwise nominal conditions). The results indicate that merely doubling d_{bc} to 6 km almost quadruples the final maximum post-loading thickness of the nitrogen ice load d_{final}, (29 km vs. 7 km for the nominal d_{bc} = 3 km case: Fig. 13b) demonstrating a highly non-linear relationship between d_{bc} and d_{final}. The stress state produced for such a model (d_{bc} = 5km, Fig. 11) resembles that for the Te = 30 km case (Fig. 7) in terms of stress magnitudes (Fig. 11A), fault type regimes, (Fig. 11B) and the extreme depth of the failed region (Figs. 11B, C), in this case penetrating the entire shell for 450 km < r_{proj} < 510 km. Cryomagmatic potential is greatly enhanced, with the critical 80 kg/m^3 value of $\Delta\rho_{efb}$ exceeded throughout the entire lithosphere for 520 km < r_{proj} < 710 km.

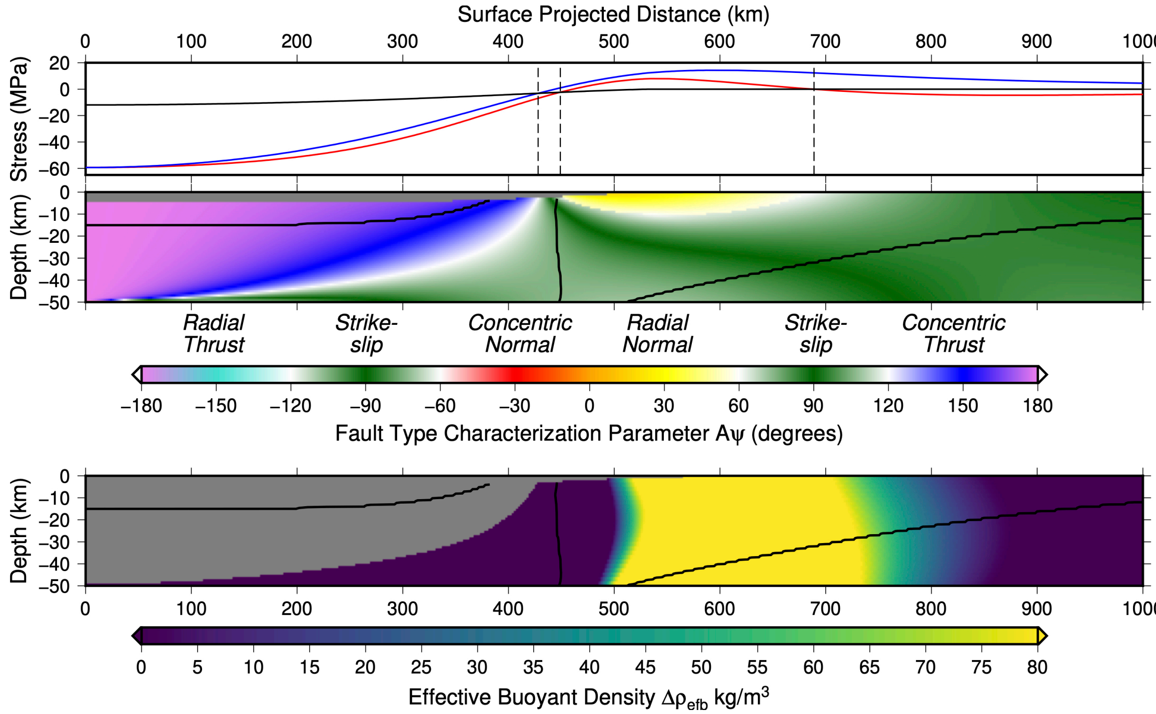

Figure 11. As in Figure 5, for model with initial basin center depth d_{bc} = 5 km. Note greater range on stress axis than previous figures.

We also consider models with an initially "bowl-shaped" basin (standard "Gaussian" shape with exponent p = 2). Such a model with otherwise nominal parameter values, including initial basin center depth d_{bc} value of 3 km, exhibits very small stress magnitudes, because the central concentration of the bowl shape results in very small load volume (Fig. 13). For a model with d_{bc} = 6 km (Figure 12), the results resemble the T_e = 70 km models in that a significant zone of concentric normal faulting regime is predicted at the surface. However, in contrast to the T_e = 70 km models, this zone occurs within a wide zone of failed shell (within the black contour on Fig. 12b), thus yielding a prediction of actual concentric normal faults being visible at the surface, a prediction that contradicts observations. The trans-basin zone of enhanced $\Delta\rho_{efb}$ values greater than the critical density offset of 80 kg/m^3 takes on an unusual "funnel" shape, wider at the bottom of the lithosphere (~140 km).

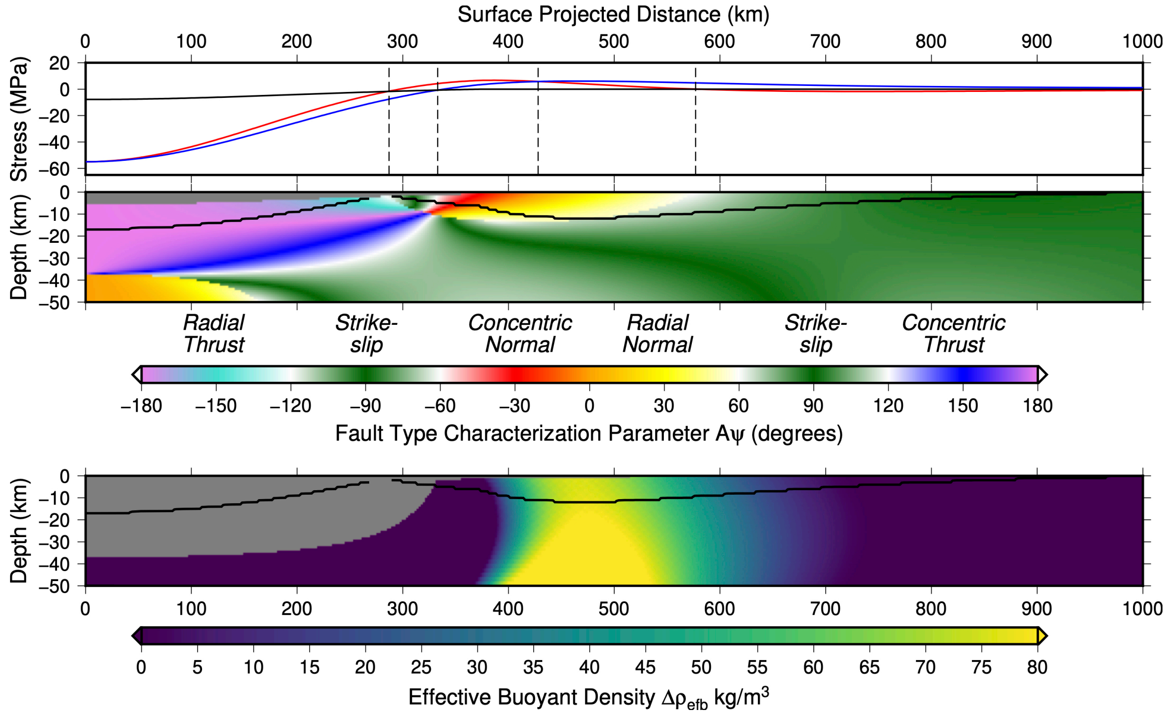

Figure 12. As in Figure 5, for model with "bowl-shaped" load and d_{bc} = 6 km. Note greater range on stress axis than previous figures.

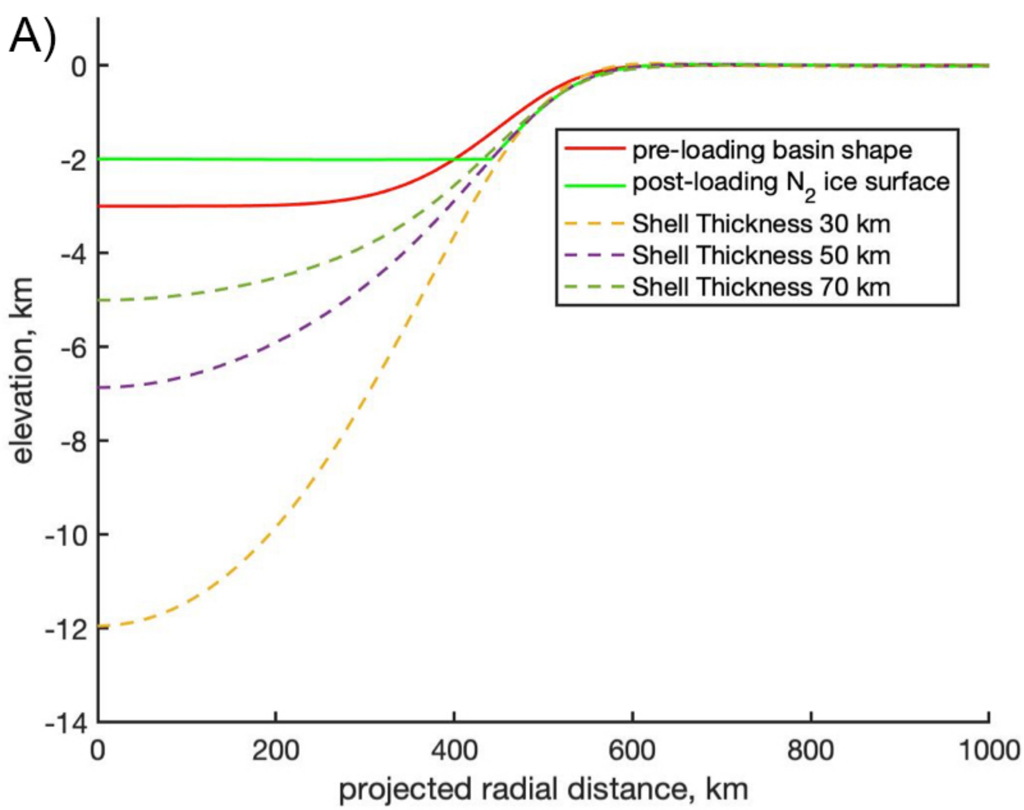

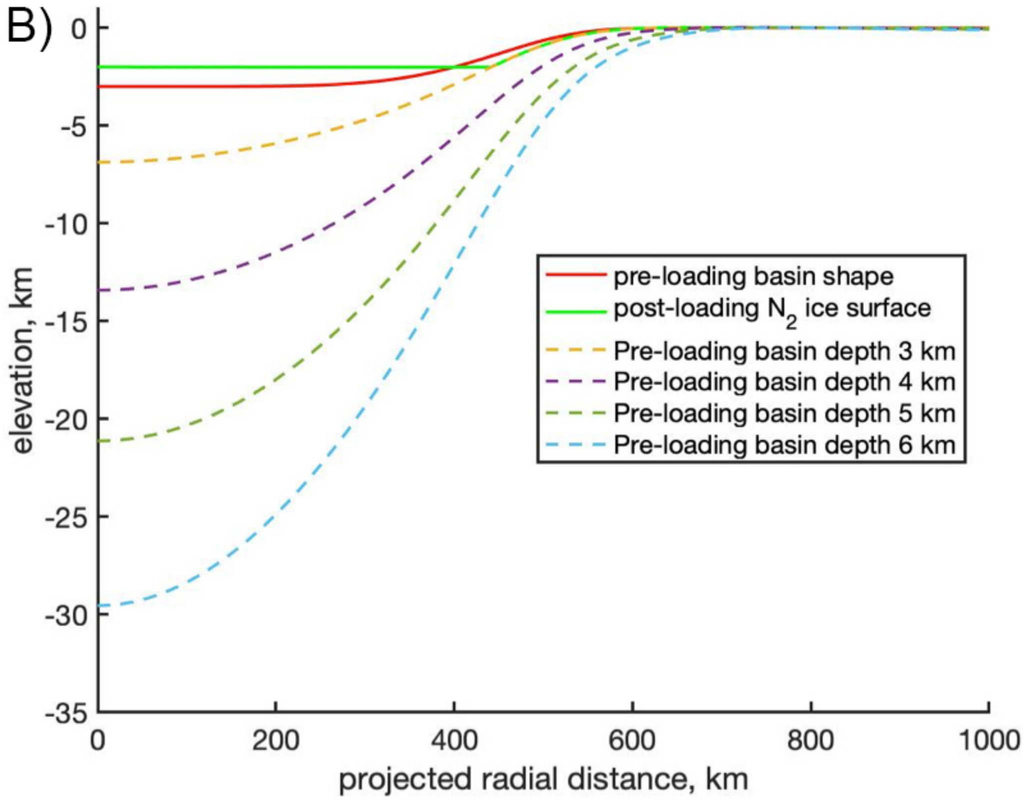
B)
0
-5
-10
-15
-20
-25
-30
-35
elevation, km
0
200
400
600
800
1000
projected radial distance, km
pre-loading basin shape
post-loading N2 ice surface
Pre-loading basin depth 3 km
Pre-loading basin depth 4 km
Pre-loading basin depth 5 km
Pre-loading basin depth 6 km

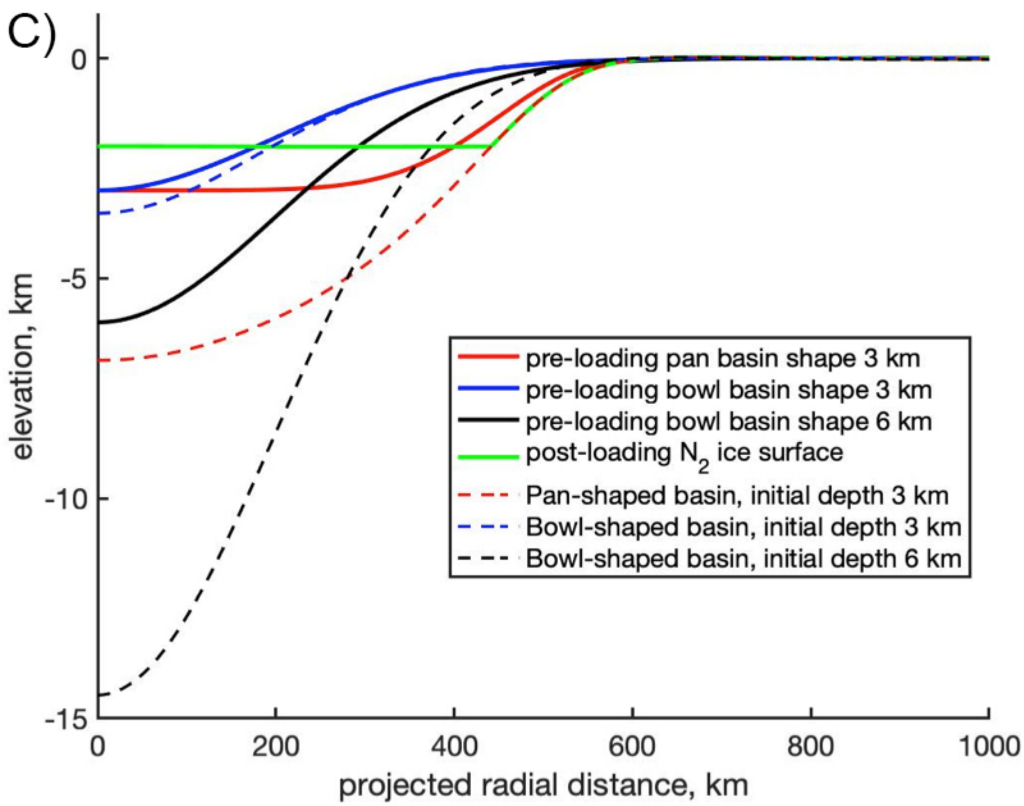
C)
0
-5
-10
-15
elevation, km
0
200
400
600
800
1000
projected radial distance, km
pre-loading pan basin shape 3 km
pre-loading bowl basin shape 3 km
pre-loading bowl basin shape 6 km
post-loading N2 ice surface
Pan-shaped basin, initial depth 3 km
Bowl-shaped basin, initial depth 3 km
Bowl-shaped basin, initial depth 6 km

Figure 13. Pre-loading (red, blue, and black solid lines) and final deformed configurations (dashed lines) of basin surface, and nitrogen ice load surface (green line, always set at -2 km elevation) for several of the models listed above. A) Dashed lines correspond to final surface positions for models with T_e of 70 km (dark green), 50 km (purple), and 30 km (yellow). B) Dashed lines show final surface position for models with initial basin center depths d_{bc} = 3km (yellow line), 4 km (purple line), 5 km (dark green line), and 6 km (blue line). C) Pre- and post-loading configurations (solid and dashed lines, respectively) for initially pan-shaped basin (super-Gaussian exponent $p = 6$) with with d_{bc} = 3 km and initially bowl-shaped basins ($p_{sg} = 2$) with d_{bc} = 3km and 6 km, (red, blue, and black lines, respectively).

6 Discussion

6.1 Overall Tectonic Pattern.

Our models give insights into the lithospheric conditions on Pluto that produce the observed distribution of faulting, fracturing, topography, and cryovolcanism in the vicinity of the Sputnik basin. As stated in section 2, the fault systems surrounding SP are characterized by a generally extensional nature and predominantly radial orientations near the rim/margins of the topographic basin, with a tendency toward more oblique orientations with increasing distance from the center of SP. Our models indicate that such conditions are favored within a fairly narrow range of elastic shell thickness, 50 ± 10 or so km. For such shells, the interaction of shell bending ("flexural") and stretching ("membrane") responses [e.g., *Turcotte et al.,* 1981] produce principal stress orientations consistent with radial normal faulting in zones up to several hundreds of km wide, corresponding to the locations of radially oriented faults around SP. Further outward in r_{proj}, stress orientations predict a transition to a strike-slip regime, and in fact over a large part of this region, intermediate $A\psi$ values lying between "pure" radial normal (30°) and strike-slip (90°) predict the presence of faults with mixed modes. In this case, the mixed mode is called "trans-tension" (e.g., Dewey et al., 1998). Evidence for such a stress regime is seen in the strike-slip duplexes of the Virgil Fossae complex (Cruikshank et al. 2019a). The main Virgil Fossae troughs are thought to be extensional faults (as mapped above), but the duplexes indicate right-lateral strike slip motion. At the duplex location, the strikes of the main Virgil Fossae faults veer counter-clockwise from radial, making an acute angle with the radial direction. The combination of these observations is consistent with a strike-slip stress regime with the most compressive horizontal principal stress oriented radial to the basin, exactly as predicted by the models of Figs. 5 and 6 (T_e = 50 km).

The predictions of the models of Figs. 5 and 6 are also consistent with the increasingly oblique-to-radial orientations of fractures seen at larger distances from SP, although it is likely that additional stress perturbations from global-scale phenomena like True Polar Wander (e.g., Keane et al., 2016) also contribute to such divergence. The greater the distance from SP's center, the more the loading stress magnitudes decline (Figs. 5A-10A), so the influence of global-scale phenomena will increase with increasing distance.

6.2 Specific Fault Systems.

The specific fault systems identified in our mapping (Figs. 2, 3) can be used to evaluate the effectiveness of our various models in representing the conditions that controlled faulting on Pluto. The "Sputnik-Radial" system (green in Figs. 1 and 14), extending from r_{proj} ~ 600 to 1600 km, exhibits dominantly radial-to-SP orientations (hence the name) with somewhat sinusoidal variations around a baseline radial trend. Such orientations in the observed locations are most consistent with our "nominal" models (Figs. 5-6). The orientation of the "West Sputnik" system (red in Figure 2) relative to SP varies considerably along its length: where the system intersects the edge of SP near 37°N 145°E, it shows predominantly radial orientations from about $r_{\mathrm{proj}} = 550$ km to 700 km, but as it progresses to the southwest, the fault strikes diverge to an oblique angle of 25° or so counter-clockwise from radial in Cthulhu Macula. As stated above, this divergence is consistent with mixed-mode trans-tensional faulting (as indicated by the $A\psi$ values in Figs. 5B and 6B), but also may reflect contributions from global-scale stress sources such as TPW (e.g., Keane et al., 2016).

The more diffuse Northwest Sputnik and East Sputnik systems (yellow and dark blue lines in Fig. 2, respectively) generally have shorter fault segments than the West Sputnik and Sputnik-Radial systems. Their fault strikes are generally quite consistent across their extents, which means that both feature zones with fault strikes that are to radial to SP (the northernmost faults in Northwest Sputnik and the southernmost ones in East Sputnik) and zones where strikes are oblique to SP (the southernmost faults Northwest Sputnik and the northernmost ones in East Sputnik). The components of these fault systems that exhibit radial orientations are consistent with the predictions of the models with T_e = 50 km (Fig. 5, 6). Components that exhibit oblique orientations indicate different conditions than for the T_e = 50 km models, which could include 1) a stress field that favors formation of obliquely oriented strike-slip faults; 2) a stress field that favors formation of concentrically oriented normal faults; and 3) inherited fabric from pre-basin stress state or fault system, and either faults were reactivated by the Sputnik basin loading stresses or new faults formed by the superposed effects of the old and new stress fields. Option 1 is consistent with the results of the T_e = 30 km models (Figs. 7, 8) in which the circum-basin failure zones are dominated by a strike-slip stress regime, suggesting that lateral variations in lithospheric thickness around the Sputnik Basin could play a role in the observed tectonic signatures. Option 2 would be consistent with the results of the T_e = 70 km models (Figs. 9, 10) in which stress regimes favoring concentric normal faults occur, again suggesting heterogeneity in shell thickness. However, the continuity of trends between the proximal and distal faults in the northern part of the East Sputnik system (Figs. 2, 3), for example, suggests a common stress field for both and not a transition from concentric normal to radial normal to strike slip as predicted in the models of Figures 9 and 10, thus casting doubt on this option. Option 3 is appealing given the broad consistent orientation trends within the Northwest Sputnik and East Sputnik systems (fractures in both systems are primarily oriented NW-SE), and the apparent continuity of the latter with faults in the basin-proximal West Sputnik system (Figs. 2, 3).

We do not consider the relationship of the Ridge-Trough System (RTS) to SP loading because of evidence that this system predates the SP impact (Schenk et al., 2018). However, it is clear that the Sputnik basin has interacted with the older RTS where the disrupted blocks of material (such as al-Idrisi Montes) are seen to break off the water ice shell and embed within the nitrogen ice (e.g., Moore et al., 2016; White et al., 2017; O'Hara and Dombard, 2021).

Crustal collar loads (Figures 6, 8, 10) also affect predictions of fault type, orientation, and lateral extent of faulting. For the T_e = 50 km case, the modeled crustal collar load (Fig. 6) both increases the depth of faulting and increases the width of the region at the surface showing a radial normal faulting regime, relative to the nominal case (Fig. 5). Both of these trends improve the correspondence of model predictions with the observed normal fault systems with dominantly radial orientations in the corresponding distance range from basin center (Figure 3). In contrast, for the T_e = 70 km models the crustal collar load instead increases the extent of the concentric normal regime zone relative to the nominal case (compare Figure 10 with Fig. 9, at odds with observed fault orientations at these distances from basin center.

In general, the observed fault distributions are inconsistent with the predictions of many of our models (with minor exceptions as pointed out above). For a thin lithosphere (T_e = 30 km, Fig. 7), almost the entire lithosphere beyond r_{proj} = 400 km is characterized by a strike-slip fault regime, save for an extremely shallow sliver (2 km depth) at the margin of the basin. This observation, coupled with the great depth of the predicted failure region (Fig. 7B, C) indicates that the faulting peripheral to the basin should have a definitive strike-slip character (including fault strikes oblique to radial), in contrast to the strongly radial nature of the observed fault systems, particularly in the r_{proj} = 500-800 km range. One potential solution to this conundrum is the possibility that all the structures identified as radial faults are actually fractures marking the surface expressions of dikes (which would be oriented perpendicular to the least compressive stress σ_ϕ and therefore radial to the basin). However, we consider this explanation to be extremely unlikely due to the lack of evidence for pervasive cryovolcanism that would result from such widespread diking. One favorable aspect of the T_e = 30 km model with respect to cryovolcanism is that the values of $\Delta\rho_{efb}$ in the region at and just beyond the basin rim easily exceed the 80 kg/m^3 threshold even without a crustal collar basal load.

For a shell with thickness T_e = 70 km, several distinct properties of the stress distribution yield predictions that strongly differ from observations. First, the fault regime at the margin of the basin is concentric normal, extending out to about r_{proj} = 550 km (Figs. 9), in contrast to the generally observed radial orientations of faults there. Second, both the horizontal stress magnitudes and the differences between them are very small (the former of order 1 MPa, the latter on the order of tenths of an MPa or less). Thus, the region of predicted failure only covers a small lateral extent, one that more or less corresponds to the surface range of the concentric normal zone, and with depth of less than 1 km at maximum. We expect almost no surface faulting from such a stress state, and those minimal faults would have the wrong orientations. A model with T_e = 70 and a crustal collar load partially ameliorates this condition, producing a region extending from 480 < r_{proj} < 790 km, with maximum depth of several km (Figure 10). However, the problem with prediction of mostly concentric normal faulting in this region remains (although the predicted mechanism of region outward of r_{proj} = 700 km becomes radial normal). Further, the enhancement of $\Delta\rho_{efb}$ for this case falls short of the 80 kg/m^3 value, averaging about 50 kg/m^3 in the mid-lithosphere.

6.3 Interplay of flexural and membrane support.

The stress and deformation of Pluto's icy shell from the nitrogen ice loading of the Sputnik basin, which are the important properties of the modeled stress states presented above, result from interplay between two important modes of lithospheric loading: a bending, or "flexure" response, and a stretching, or "membrane" response (Turcotte et al., 1981; Janes and Melosh, 1990; Banerdt et al., 1992). In general, a membrane-type response becomes more prominent with increasing contribution of sphericity to the response [e.g., Turcotte et al., 1981], a function of the ratio of characteristic load width to planetary radius (which can also be expressed as degrees of arc). However, some amount of stretching response can be seen in planar-geometry flexure solutions as well, particularly for more physically complete "thick plate" formulations (e.g., Comer, 1983). Nonetheless, membrane stress components induced by Sputnik basin-sized loads can exert a primary control on the tectonic expression of a planet, primarily through the extensional contribution to the out-of-plane stress (see below).

Both flexure and membrane responses are considered "tectonic" stress components as defined above, because they are superposed on the general state of stress induced by gravity, which we assume to be lithostatic here Bending of an elastic plate produces a characteristic "dipole" tectonic stress response, with maximum values of horizontal tectonic stress at the top and bottom (of opposite sign), with a "neutral plane" of zero stress in the middle. The dipole is the manifestation of a vertical gradient in horizontal normal stress in the absence of any stretching response. In contrast, the tectonic stresses induced by a stretching response are constant through the thickness of the lithosphere. This interplay is demonstrated in Figure 14B: the deviations from vertical (or, gradients) in the tectonic stress components represent flexural contributions, and the positions with respect to the zero-stress coordinate reflect the membrane contributions. Note that the horizontal in-plane stress components (σ_{Th}, red lines) tend to have the larger gradients, and are thus more influenced by the bending response, whereas the out-of-plane components ($\sigma_{T\phi}$, blue lines) tend to be vertically more flat, and are therefore more influenced by membrane support. Further, note that the entireties of the $\sigma_{T\phi}$ components in. Fig. 14 are on the extensional (positive) side. This phenomenon is a main driver of both the radial normal fault regime zones seen in Figures 5B and 6B and the facilitation of radial orientations for dikes beyond the basin, allowing the enhanced magma ascent potential seen in Figures 5C and 6C to be realized.

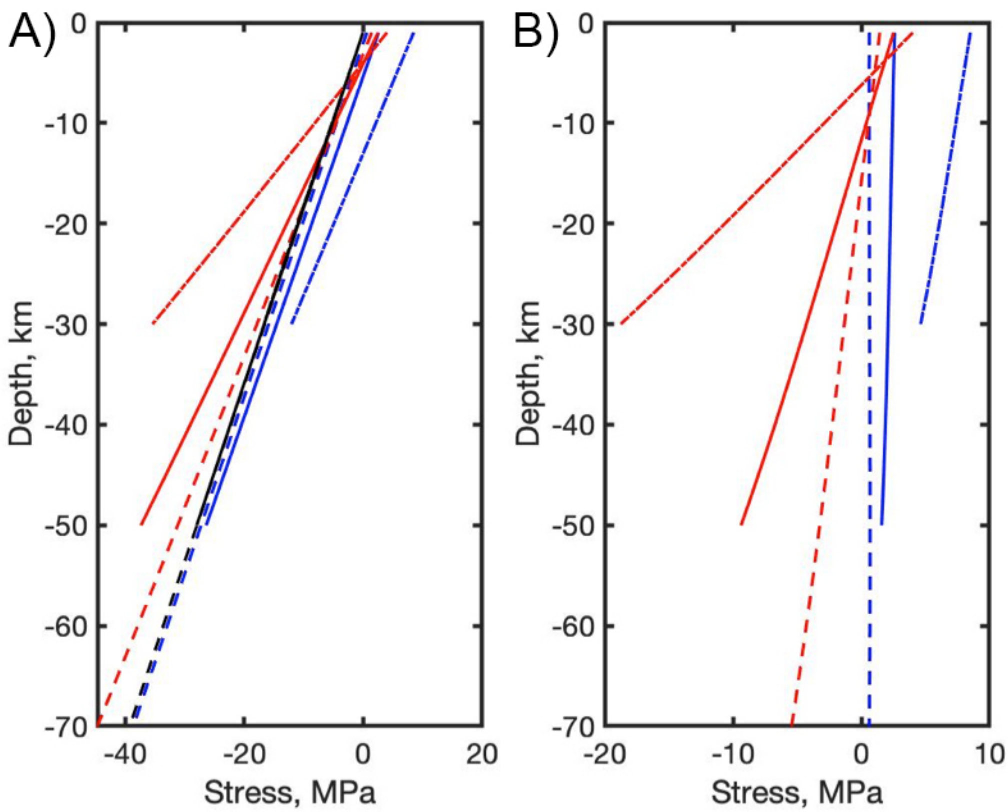

Figure 14. Vertical profiles (at r_{proj} = 478 km) of horizontal stress components in model lithospheres, to demonstrate the interactions of the flexural and membrane stresses in creating the tectonic predictions and the cryovolcanic enhancement. (A) Full (i.e., including lithostatic contributions) stress components σ_h (red) and σ_ϕ (blue) vs. depth for models with T_e = 30 (dash-dot lines) 50 km (solid lines), and 70 km (dashed lines). Vertical normal stress σ_z shown as black lines. (B) Vertical profiles of tectonic stress (vertical minus horizontal, essentially removing the lithostatic contributions) components σ_{Th} (in-plane, red lines) and $\sigma_{T\phi}$ (out-of-plane, blue lines), with dashed and solid lines as in A.

Many planetary loads that cause downward flexure are of modest lateral extent relative to the planetary radius: for example, volcanic edifices on large planets such as Earth and Venus (e.g., McGovern, 2007; McGovern and Solomon, 1998) and volcanic fill of impact basins on the Moon (e.g., Mare Serenitatis, in Solomon and Head 1979). For such loads, the in-plane horizontal normal stress (called σ_h here) is the most tensile one, leading to a favored concentric orientation of extensional faults (graben). In constrast, stretching of a spherical shell produces components of horizontal normal stress that are constant with vertical position in the shell. For sufficiently wide downward loads on elastic spherical shells, the out-of-plane normal stress σ_ϕ is the most extensional, leading to a predicted radial orientation of graben (e.g., Turcotte et al., 1981; Sleep and Phillips, 1985; Banerdt et al., 1992).

Variations in model parameters can affect the balance of the flexural (bending) and membrane (stretching) responses: in general, the response is governed by whichever mechanism provides the most resistance to deformation. We find that low values of T_e and high values of characteristic load width favor the membrane response, and high values of T_e and low values of characteristic load width favor the flexure response. The analysis of Turcotte et al. (1981) reveals the physical basis for these results: the parameter σ that measures the resistance to bending is proportional to T_e to the third power, whereas the parameter τ that measures the shell's resistance to deformation if bending is neglected (i.e., the membrane response) is merely proportional to T_e. Thus, the ratio σ/τ is proportional to T_e^2, demonstrating that increasing T_e will greatly increase the resistance to bending relative to the resistance to membrane deformation, leading to an increasingly bending-dominated response (being the stronger mechanism). Comparing Fig. 7 (T_e = 30 km model) and Fig. 9 (T_e = 70 km model) demonstrates this effect: the former is nearly uniformly characterized by the strike-slip regime generated by the extensional σ_ϕ characteristic of the membrane response. We also note an apparent paradox: while low lithospheric thickness is stated above to favor a membrane response, the low-thickness T_e = 30 case (Fig. 5) exhibits high stress gradients (Fig. 14B), a characteristic linked to flexural response. Conversely, the high-thickness T_e = 70 km case (Fig. 7), favoring a flexural response, exhibits low stress gradients, a characteristic of a membrane response. These findings are in fact a natural consequence of the amount of support provided by each response under situations where both contribute: flexural deformation and stress gradients increase with decreasing T_e, so the T_e = 30 km case will have the highest gradients (Fig. 14B), although the magnitude of the offset toward extension of the $\sigma_{T\phi}$ curve shows the dominant influence of the membrane response in setting the tectonic state. Conversely, the T_e = 70 km case shows the lowest gradients (Fig. 14B), reflecting a high level of support, but the greatly reduced magnitudes of the lateral offsets relative to the other thickness cases show the diminishing influence of the membrane response.

The combination of lithospheric bending and stretching phenomena creates the distinctive features of our models. For example, the "crescent" of upper lithosphere fault regime zones is the result of the combination of a flexural stress gradient (resulting in differing stress conditions at the top and bottom of the lithosphere) with extensional components of membrane stress that vary in such a way to (generally) yield normal faulting regimes near the margin of the basin and a strike-slip regime in the surrounding regions. However, interactions between the lithospheric thickness and the shape of the load(s) also play roles here. For example, the almost complete lack of normal faulting in the T_e = 30 km model (Figs. 7, 8) shows the dominant membrane nature of the response for thin lithospheres; only for a limited range of r_p does σ_h become extensional in the uppermost several km of the shell (joining the higher σ_ϕ), a requirement to depart the strike-slip regime.

The work of Janes and Melosh (1990) illuminates considerations of the relative contributions of flexural and membrane loading to planetary tectonics. Consider the first sentence of their abstract: “The tectonic response of a planet's lithosphere to an imposed load contains information on the mechanical properties of the lithosphere, particularly its thickness...", a statement that encapsulates the approach we have taken in this manuscript. Janes and Melosh (1990) calculated tectonic states from surface stress components using a general model of spherical shell loading (i.e., containing both flexural and membrane components) capable of handling arbitrary shell thicknesses. These workers characterized the surface tectonic signatures of end member flexure and membrane responses, and also a "transition" response between them, for typical large (Mars) and small (Uranus's moon Miranda) planets that exhibit differing values of a support parameter q. The far-field response (radial normal fault regime) to a Sputnik Planitia-filling load at T_e = 50 km (Figure 5) corresponds to the predicton of the Janes and Melosh (1990) “transition” response for a small planet with intermediate thickness lithosphere (see the upper right portion of Figure 8b of that paper). For a reduced lithospheric thickness (T_e = 30 km, Figure 7), the trans-basin response is instead dominated by a strike-slip regime, corresponding to the “transition” prediction for a thinner lithosphere in Figure 8b of Janes and Melosh (1990). Note that the appearance of a small and shallow radial normal regime zone in our T_e = 30 km model is a result of a small positive excursion of σ_r between $r_p \approx 400$ and 560 km (Figure 7A); such an excursion is a departure from the always-negative σ_r “membrane” loading state, and likely results from a combination of differences in load shape and support parameter q between the respective models.

6.4 Elastic thickness of Pluto’s ice shell.

Models with elastic shell thicknesses T_e significantly different from 50 km produce predictions of tectonic state that differ significantly from the observed predominantly radial normal faulting state. Thus we conclude that the thickness of the elastic part of Pluto’s ice shell during the time that the bulk of the nitrogen ice loading occurred is 50 ± 10 km, adjoining the estimate of T_e of 60 km from limb profile topography (Conrad et al., 2021). This relatively close correspondence suggests that the time periods over which the topographic features observed on the limbs formed and the nitrogen ice load was emplaced overlapped to some extent, but does not require overlap if a quasi steady-state shell thickness was reached at some point in Pluto's evolution.However, the range of our results below 60 km suggests a generally warmer Pluto interior and higher thermal gradient that found by Conrad et al. (2021).

6.5 Sub-ice-load stress state.

Model stress states predict thrust faulting of ambiguous orientation in the interior of the load region (Figs. 5-12). However, evidence for compressional tectonics per se is lacking at the surface of the materials filling Sputnik basin. The morphology of the nitrogen ice materials is controlled by solid-state flow at current Pluto surface conditions (Trowbridge et al., 2016; McKinnon et al., 2016; Urmurhan et al., 2017; Wei et al., 2018) that will tend to remove tectonic evidence of lithospheric stresses, in contrast with, say, basin-filling lunar mare basalts, which do not flow at lunar surface conditions and therefore display tectonic features consistent with predicted lithospheric stress states [e.g., Solomon and Head, 1980]. This is similar to the effect that detached basal boundaries have on volcano tectonics [e.g., McGovern and Solomon, 1993, 1998; McGovern and Morgan, 2009], in that transmission of horizontal compressive flexural stresses from the lithosphere into the load is inhibited by a slip boundary condition between lithosphere and load, but with the added difference that the nitrogen ice load itself removes internal differential stresses via ductile flow.

6.6 Topographic constraints: rim.

The Sputnik basin exhibits prominent rim topography that is particularly well defined in the west profiles (Figs. 4B, 15). Impact basin rim topography can arise from the response to the impact process, including structural uplift and overturn of the target rock and emplacement of ejecta at the surface (e.g., Melosh, 1989). The extent to which post-impact lithospheric loading plays a role in generating a rim signature can be evaluated by the results of our models. Models in which the sole loading is within the basin (e.g., Figs. 5, 7, 9, 11, 12) do not generate a significant topographic signature at the position of the basin (see the blue dashed line in Figure 15). Note that this result is counter to the prediction of substantial topographic "arches" generated by flexure models that neglect the effects of lithospheric curvature (e.g., Mills and Montesi, 2019). The difference results from the relatively low amount of support from flexural bending, the main arch-producing mechanism (and the origin of the term "flexural arch"), for loads of SP's dimensions on a planet of Pluto's size.

However, uplift resulting from a crustal collar load can produce topography at the basin margin that at least partially resembles the observed topographic profiles (Figure 15). For elastic thicknesses at the middle of our preferred range (T_e = 50 km), uplift from the crustal collar load produces a broad swell spanning from the basin margin to $r_p \approx 900$ km. These model swells overlap with two prominent topographic highs in the west basin profiles (Figs. 4B, 15): the aforementioned rim and a second outer high located between about $r_p \approx 750$ and 830 km. The model profiles could plausibly contribute to the relief seen at these highs, and the outward-facing slope of the outer high is echoed in the model profiles. Of course, the prominent low between these highs disrupts the fits. However, this low likely reflects another critical aspect of the impact process: an outer basin ring (e.g., Melosh, 1996; Spudis, 1993, McKinnon et al., 2017), marked by the highest point of the outer high. Thus, it is reasonable to evaluate the fit at only the topographic highs. We conclude that uplift from a crustal collar load can contribute to the observed topographic profiles of the Sputnik basin and its surroundings, although this is not a required element given the other potential relief-generating mechanisms (e.g., McKinnon et al., 2017).

The response of the lithosphere exerts strong controls on the possible range of crustal collar topographic expressions. The characteristic width of the uplift profile is not substantially affected by the width of the actual crustal collar load: compare the results for the nominal width (brown dashed line) and narrow (yellow dashed line) crustal collar loads at T_e = 50 km in Fig. 15, for which the main difference is the lower height reached by the narrower (and therefore weaker) load. Thus, we conclude that the uplift wavelength is set by the response of the lithosphere, which effectively filters the wavelength of the load: thinner lithospheres will produce shorter uplift wavelengths. Also note that the best overall fit to the main rim and outer high (including outward-facing slope) comes from the T_e = 30 km crustal collar model, with its shorter wavelength response. However, this best fit would presume that no other process contributed to positive rim topography at the Sputnik basin, an unlikely scenario, and in any event this T_e value can be rejected for the other reasons outlined above.

6.7 Topographic constraints: initial basin depth.

The initial depth of the basin is also constrained by the topography. The central depth of fill d_{final} required to match the observed -2 km elevation offset increases non-linearly with increasing initial basin depth d_{bc}, such that merely doubling d_{bc} for the T_e = 50 km model quadruples d_{final}. This strong non-linearity is a consequence of the compensating lithospheric deformation resulting from a given amount of applied load: adding a load thickness increment increases the resulting surface elevation of the load by only a fraction of this increment, determined by the interplay of flexure and membrane responses as described above. On Pluto, this phenomenon is exacerbated by the extremely low compensating density contrast between shell and ocean that results in high compensating deflections relative to, say, silicate-dominated planets with large crust-mantle density contrasts. Such "diminishing returns" on thickness increments means that a maximum nitrogen ice thickness reaching several tens of km is required for basins with d_{bc} greater than 4 km. Such values of nitrogen ice thickness are unlikely on several grounds, not least that this depth is much deeper than any likely impact basin, especially as the surface of SP is already at least 2-3 km below the surrounding terrain (McKinnon et al., 2016). Thus, we suggest that the original depth of the basin at the time of initiation of nitrogen ice infill cannot be significantly deeper than 3 km. Such a finding is consistent with the "warm" Pluto SP impact models of Johnson et al (2016), with post-response depths of several km, and inconsistent with the "cold" Pluto models in the same work (initial depths of 10s of km) unless significant post-impact relaxation of topography occurred. If Pluto remained cold, such relaxation would be unlikely. Our results are also therefore consistent with the "hot" start and early ocean formation for Pluto found by *Bierson et al.* (2020).

Our models also show another primary reason why the *initial* shape of the Sputnik basin must be pan-shaped and shallow (less than 4 km): the amount of fill required to meet the surface topography constraint is so large that the lithosphere would be pervasively faulted in a dominantly strike-slip mode (Fig. 11), contradicting the observed limited amount of fracturing and its dominant radial extension nature. The problem is exacerbated by the added thinning of the central shell that deeper basins represent, yielding more deformation and stress for a given load amount. Further, possible stress/deformation ameliorating factors such as thicker lithosphere (Figs. 9-10) are not viable because models with those properties fail to match observed faulting geometries.

The elevation offset of -2 km also provides a constraint on the minimum initial depth of the basin. For a pan-shaped basin with d_{bc} < 2.2 km, there is no solution that allows a –2 km offset, as the final relief built up within the basin will always exceed that topographic level. In the limit of no initial basin topography (the favored hypothesis of Hamilton et al., 2016), only positive relief features (essentially mountains) can result from emplacement of material with the density of nitrogen ice. In order for this scenario to match the observations, several (perhaps ranging into the high single digits) kilometers of nitrogen ice would have to be removed while more or less maintaining the underlying lithospheric deflection profile caused by the original load. Since the fluid providing the basal restoring force (the water ocean) has very low viscosity, reponse to load removal will be nearly instantaneous, such that a time lag between nitrogen ice load removal and basin readjustment cannot be invoked to create this situation. Thus, to create and preserve an offset, the "no initial basin" scenario requires both partial removal of the load and an increase in elastic shell thickness between times of original load emplacement and partial load removal; Hamilton et al. (2016) invoke an early epoch of "thin" lithosphere in order to facilitate creation of a deep depression from deposited nitrogen ice. Nonetheless, an "initially flat" scenario must conform to the constraints laid out above, which include a T_e value *at the time of nitrogen ice loading* of about 50 km. The "no initial basin" scenario would therefore require a current-day T_e value well in excess of 50 km, implying a high rate of internal cooling for Pluto. Further, a "no initial basin" scenario cannot explain the current elevated rim of the Sputnik basin (Figure 4), since loading will not produce such a topographic signature (Figure 13). However, the impact process itself, and subsequent deformation resulting from impact-generated loads like crustal collars, are capable of producing rim topography. Thus, the results reported here favor the interpretation of Sputnik Planitia as the site of an impact basin.

Finally, we note that the *final* shape of modeled basins tends towards a bowl shape, regardless of whether the initial shape was bowl-like or pan-like. For initially pan-shaped basins, the downward deflection of the lithosphere tends to remove the flat central topographic signature; compare the initial and final configurations of the nominal pan-shaped basin model (red lines) in Fig. 13C. This is a quite simple consequence of the long-wavelength natures of both flexure and membrane responses, with the greatest deflections near the center of the load and decreasing outward in r_{proj}. Any initially flat surface will inevitably be tilted inward toward the center of the basin by such a response, and a curved shape characteristic of loading-induced subsidence will be reflected in the final basin surface configuration.

6.8 Cryomagmatism.

Stress gradients for models with lithospheres with $T_e \geq 70$ km (e.g., Figs. 9, 10) are too low to provide any significant enhancement of cryomagma ascent in the regions surrounding the basin. Thus, if lithospheric stresses have aided cryomagma ascent around SP, we can infer that Pluto's T_e is less than about 60 km, a value also consistent with the dominantly radial extensional tectonic modes surrounding SP (see the "elastic thickness" section above). As described in section 1, proposed sites of cryomagmatism include Hekla Cavus, Viking Terra, Pioneer Terra, Virgil Fossae, Wright Mons, and Piccard Mons (at distances 527, 582, 815, 900, 957, and 1254 km from the center of SP at 25°N, 175°E, respectively). The first three fall into radial ranges that overlap with zones of enhanced magma ascent in one or more or our models (Figs. 5-12), but the two Montes and Virgil Fossae fall beyond the zones with peak enhancement ($\Delta\rho_{efb} > 80$ kg/m^3). In the cases of Wright and Piccard Montes, they are closer to the south-southeast extension of SP, a zone of loading that might become a significant or even primary influence in that region, suggesting the need for further non-axisymmetric models. Virgil Fossae lie on a system of fractures oriented radially to SP, suggesting that the observed cyromagmatism could reflect down-strike transport in an underlying dike connected to the enhanced zone.

6.9 Existence of crustal collar loads.

Crustal collar loads are suggested by impact hydrocode models, are detected by gravity at lunar basins, and are implicated in the origin of mascon gravity signals. This load appears necessary to explain rim topography, since the low amount of flexure for this load configuration will not produce much of the observed rim topography, although some of that topography is likely due to ejecta (McKinnon et al., 2017). But the timescale of response to crustal collar loads for basaltic planets is determined by the relaxation time of the underlying mantle. Under our lithospheric modeling scheme, an icy planet's ocean (as the fluid substrate to the shell) is the equivalent of the mantles of silicate planets. However, the difference between silicate mantles and Pluto's ocean "mantle" is that the latter has a very low viscosity, such that the response would be more or less instantaneous, versus the drawn-out response times of the former (typically 10^3-10^6 years for Earth's mantle). Thus, the time scale of the impact response becomes relevant. In hydrocode models, the largest deformation occurs plastically, whereas the models in this paper consider elastic response to loading. If for some reason the surface material reaches its final post-impact configuration before the subsurface crustal collar does, then the response we are modeling here is relevant. If the surface material reaches this configuration after the collar does, then this loading would not have the same effect as modeled (although some topographic effect might be seen). If the timescales are the same, it is plausible that the crustal collar models presented here are relevant.

6.10 Basaltic Planet Analogs for Basin-flanking Volcanism.

Here we have proposed that the emplacement of cryovolcanic centers in the region surrounding the Sputnik basin has been facilitated by lithospheric stresses induced by the basin-filling nitrogen ice load. However, associations of volcanic provinces with large impact basins have long been noted on the silicate planets Mars and the Earth's Moon, and McGovern (2018) proposed that similar stress-based magma ascent enhancement has occurred at these locations. Specific examples of such provinces include the Circum-Hellas Volcanic Province (CHVP) on Mars (Williams et al., 2009) and Mare Tranqullitatis, located within the triangle formed by the Crisium, Serenitatis, and Nectaris basins on the Moon (Litherland and McGovern, 2009; McGovern and Litherland, 2011; McGovern et al., 2013). Preservation of such provinces to the present day requires that the surface signatures of large basins and their surroundings not be removed by vigorous resurfacing that evidently characterized the larger silicate planets Earth and Venus, thereby limiting such evidence to the smaller planets, sometimes termed "one-plate planets" (Solomon, 1975). The Kuiper Belt object Pluto evidently shares such preservation of the early solar system impact record.

6.11 Future Directions.

Despite the progress on understanding Sputnik Planitia and its surroundings presented here, there remain ample opportunities for improvement. Future work on the Sputnik basin can address some of the limitations of the models presented above. For example, the significant departure of the SP nitrogen ice unit from axial symmetry in the south-southeastern extension of the main basin, which may reflect an elliptical basin shape or irregular low-angle impact geometry, is unaccounted for here. While we do not expect accounting for such variations to substantially change the main conclusions reached here regarding lithospheric thickness and basin dimensions, implementing models that account for non-axisymmetric shape of SP could address in particular the role of loading in enhancing cryomagmatic potential at the locations of the prominent Wright and Picard Montes. A 3-Dimensional approach can account for such asymmetries, allowing for explicit calculation of tectonic and topographic expressions from the full extent of the nitrogen ice load (e.g., McGovern et al., 2020). Calculation of time-dependent responses to loading can also increase our understanding. For example, implementing viscoelastic rheology would allow the response of the whole shell to be accounted for, including the warm ductile lower regions. Further, models with plastic rheology can account for the stress relief from brittle failure (faulting), allowing for a more self-consistent evolution of the surface and interior stress states.

7 Conclusions

The fault systems that surround the Sputnik basin are critical clues to the characteristics of the mass of nitrogen ice that fills the basin and to the properties of Pluto's icy shell lithosphere. Numerical models of nitrogen ice loading within SP predict distributions of faulting with mechanisms (dominantly normal, but with some transtensional contributions) and orientations (dominantly radial, with increasing obliquity with increasing distance from the basin center) that match the observed distributions of tectonic features surrounding SP. These distributions are strongly diagnostic of the elastic thickness of Pluto's spherical ice shell: preferred values fall in the range 50 ± 10 km. Models with elastic ice shell thicknesses significantly different from 50 km produce predictions of tectonic state that differ significantly from the observed predominantly radial normal faulting state. The initial depth of the basin is also constrained by the topography. The required depth of fill increases non-linearly with increasing initial basin center depth d_{bc}, such that merely doubling d_{bc} for the T_e = 50 km model sextuples the load thickness required to reach the observed -2 km elevation offset. Thus, we suggest that the original depth of the basin cannot be significantly deeper than 3 km, a finding consistent with the "warm" Pluto SP impact models of Johnson et al (2016), and therefore also with the "hot" Pluto origin of Bierson et al. (2020). We also find that the initial basin cannot be shallower than 2.2 km; otherwise the elevation offset could not reach -2 km depth. This finding rules out scenarios for which there was no pre-existing basin (e.g., the favored scenario of Hamilton et al., 2016), barring a fortuitous combination of shell thickness evolution and load erosional history. Uplift generated by a "crustal collar" load may contribute to part of the observed topographic signal of the basin and its surroundings. The combination of extensional out-of-plane lithospheric stress and positive vertical gradients of tectonic stress generated by the loading creates an enhancement of cryomagma ascent in dikes in an annular region surrounding the basin, corresponding to the locations of many prominent sites of proposed cryovolcanism on Pluto.

Acknowledgments, Samples, and Data

We acknowledge support from NASA NFDAP program grant 80NSSC18K1317 (to P.I. McGovern). We are grateful to the New Horizons Mission Team for their enormous accomplishments in collecting the incredible Pluto datasets used in this study.

The base maps we used include the LORRI-MVIC global mosaic and the global stereo digital elevation model of Pluto, both projected at 300 m/pixel. These are archived in the PDS Imaging and Cartography Node, and can be downloaded at the following links:

Global mosaic:

https://astrogeology.usgs.gov/search/map/Pluto/NewHorizons/Pluto_NewHorizons_Global_Mosaic_300m_Jul2017

Global DEM:

https://astrogeology.usgs.gov/search/map/Pluto/NewHorizons/Pluto_NewHorizons_Global_DEM_300m_Jul2017

References

Ahrens C. J. and Chevrier V.F., 2021. Investigation of the morphology and interpretation of Hekla Cavus, Pluto. *Icarus, 356*, 114108.

Andrews-Hanna, J. C., 2013. The origin of the non-mare mascon gravity anomalies in lunar basins, *Icarus, 222*, 159–168.

Bertrand T. and Forget F. (2016) Observed glacier and volatile distribution on Pluto from atmosphere-topography processes. *Nature*, *540*, 86-89.

Bertrand T., Forget F., Umurhan O. M., et al. (2018) The nitrogen cycles on Pluto over seasonal and astronomical timescales. *Icarus*, *309*, 277-296.

Bierson C. J. et al. (2018) Implications of the observed Pluto-Charon density contrast, *Icarus, 309*, 207-219, doi:10.1016/j.icarus.2018.03.007

Bierson C. J. et al. (2020) Evidence for a hot start and early ocean formation on Pluto, *Nature Geoscience, 13* , 468-472, doi:10.1038/s41561-020-0595-0

Cheng A. F., Weaver H. A., Conard S. J., et al. (2008) Long-Range Reconnaissance Imager on New Horizons. *Space Science Reviews*, *140*, 189-215.

Comer R. P. (1983) Thick plate flexure. *Geophys. Journ. Int.*, *72*, 101-113.

Conrad J. W. et al. (2021) Heat Flux Constraints from Variance Spectra of Pluto and Charon from Limb Profile Topography, J. Geophys. Res. (Planets) 126, e2020JE006641, doi:10.1029/2020JE006641

Cruikshank D. P., Umurhan O. M., Beyer R. A., et al. (2019a) Recent cryovolcanism in Virgil Fossae on Pluto. *Icarus*, *330*, 155-168.

Cruikshank, D. P., Materese, C. K., Pendleton, Y. J., et al. (2019b) Prebiotic chemistry of Pluto. *Astrobiology*, *19*, ast.2018.1927.

Cruikshank D. P., Dalle Ore C. M., Scipioni F., et al. (2021) Cryovolcanic flooding in Viking Terra on Pluto. *Icarus*, 113786.

Dalle Ore C. M., Cruikshank D. P., Protopapa S., et al. (2019) Detection of ammonia on Pluto's surface in a region of geologically recent tectonism. *Science Advances*, *5*, eaav5731.

Dewey, J. F., et al. (1998) Transpression and transtension zones, in Holdsworth, R. E., Strachan, R. A. & Dewey, J. E (eds), Continental Transpressional and Transtensional Tectonics. Geological Society, London, Special Publications, 135, 1-14.

Freed, A. M., H. J. Melosh, and S. C. Solomon (2001) Tectonics of mascon loading: Resolution of the strike-slip faulting paradox. *J. Geophys. Res., 106*, 20603-20620.

Freed A. M., Johnson B. C., Blair D. M., Melosh H. J., Neumann G. A., Phillips R. J., Solomon S. C., Wieczorek M. A., and Zuber M. T. (2014) The formation of lunar mascon basins from impact to contemporary form. *J. Geophys. Res. Planets*, *119*, 2378–2397.

Galgana G. A., McGovern P. J., and Grosfils E. B. (2011) Evolution of large Venusian volcanoes: Insights from coupled models of lithospheric flexure and magma reservoir pressurization. *J. Geophys. Res. Planets*, *116*, E03009.

Galgana G. A., Grosfils E. B., and McGovern P. J. (2013) Radial dike formation on Venus: Insights from models of uplift, flexure and magmatism. *Icarus*, *225*, 538-547.

Giese, B., R. Wagner, H. Hussmann, G. Neukum, J. Perry, P. Helfenstein, and P. C. Thomas (2008) Enceladus: An estimate of heat flux and lithospheric thickness from flexurally supported topography. *Geophys. Res. Lett, 35*, doi:10.1029/2008GL036149.

Grundy W. M., Binzel R. P., Buratti B. J., et al. (2016) Surface compositions across Pluto and Charon. *Science*, *351*, aad9189.

Hamilton D. P., Stern S. A., Moore J. M., Young L. A., and the New Horizons Geology, Geophysics & Imaging Theme Team (2016) The rapid formation of Sputnik Planitia early in Pluto's history. *Nature*, *540*, 97-99.

Hammond N. P., Barr A. C., and Parmentier E. M. (2016) Recent tectonic activity on Pluto driven by phase changes in the ice shell. *Geophys. Res. Lett.*, *43*, 6775-6782.

Howard A. D., Moore J. M., White O. L., et al. (2017) Pluto: Pits and mantles on uplands north and east of Sputnik Planitia. *Icarus*, *293*, 218-230.

Hurford, T. A., R. A. Beyer, B. Schmidt, B. Preblich, A. R. Sarid, R. Greenberg (2005) Flexure of Europa's lithosphere due to ridge-loading. *Icarus, 177*, 380-396.

Janes, D. M. and Melosh H. J. (1990) Tectonics of Planetary Loading: A General Model and Results, *J. Geophys. Res., 95*, 21,345-21,355.

Johnson B. C., Bowling T. J., Trowbridge A. J., and Freed A. M. (2016) Formation of the Sputnik Planum basin and the thickness of Pluto's subsurface ocean. *Geophys. Res. Lett.*, *43*, 10,068-10,077.

Keane J. T., Matsuyama I., Kamata S., and Steckloff J. K. (2016) Reorientation and faulting of Pluto due to volatile loading within Sputnik Planitia. *Nature*, *540*, 90-93.

Kimura, J., and S. Kamata (2020), Stability of the subsurface ocean of Pluto, *Plan. Spa. Sci. 181*, 104828, doi:10.1016/j.pss.2019.104828

Litherland, M. M., and P. J. McGovern (2009) Effects of planetary radius on lithospheric stresses and magma ascent on the terrestrial planets, *Lunar Planet. Sci., 40,* abstract 2201.

McGovern, P. J., and S. C. Solomon (1998) Growth of large volcanoes on Venus: Mechanical models and implications for structural evolution, *J. Geophys. Res., 103*, 11,071-11,101.

McGovern, P. J. (2007) Flexural stresses beneath Hawaii: Implications for the October 15, 2006, earthquakes and magma ascent, *Geophys. Res. Lett., 34*, L23305, doi:10.1029/2007GL031305.

McGovern, P. J., and M. M. Litherland (2011), Lithospheric Stress and Basaltic Magma Ascent on the Moon, with Implications for Large Volcanic Provinces and Edifices, *Lunar Planet. Sci., 42*, abstract 2587.

McGovern, P. J., W. S. Kiefer, G. Y. Kramer, M. T. Zuber, J. C. Andrews-Hanna and J. W. Head III (2014), Magma ascent at lunar impact basins: Effects of lithospheric tectonic stress gradients, brittle failure, and volatile generation, 45th Lunar and Planetary Science Conference, abstract 2771.

McGovern, P. J. (2018) Intra- and trans-(impact) basin igneous provinces on the Moon and Mars: Signposts of broad-scale primordial events, 49th Lunar and Planetary Science Conference, abstract 1814, 2018.

McGovern P. J., White O. L., and Schenk P. M. (2019) Tectonism across Pluto: Mapping and interpretations. *Pluto System After New Horizons 2019*, Laurel, MD, Abstract #7063.

McGovern P. J., White O. L., and Schenk P. M. (2020) Global Tectonics of Pluto: The Roles of Basin Infill Loading and True Polar Wander, AGU Fall Meeting 2020 abstract.

McKinnon W. B., Nimmo F., Wong T., et al. (2016) Convection in a volatile nitrogen-ice-rich layer drives Pluto's geological vigour. *Nature*, *534*, 82-85.

McKinnon W. B., Schenk P. M., Mao X., et al. (2017) Impact Origin of Sputnik Planitia Basin, Pluto. *Lunar Planet. Sci. Conf. XLVIII*, Abstract #2854.

Melosh H. J. (1996) *Impact Cratering: A Geologic Process*. 245 pp. Oxford University Press.

Melosh H. J., et al. (2013) The origin of lunar mascon basins. *Science*, *340*, 1552–1555, doi:10.1126/science.1235768.

Mills A. C. and Montési L. G. J. (2019) Elastic Flexure Around Sputnik Planitia, Pluto, and Evidence for a Very High Heat Flux. *Pluto System After New Horizons 2019*, Laurel, MD, Abstract #7030.

Moore J. M., McKinnon W. B., Spencer J. R., et al. (2016) The geology of Pluto and Charon through the eyes of New Horizons. *Science*, *351*, 1284-1293.

Moore J. M., Howard A. D., Umurhan O. M., et al. (2018) Bladed terrain on Pluto: Possible origins and evolution. *Icarus*, *300*, 129-144.

Moruzzi S. A., Andrews-Hanna J. C., and Schenk P. (2021) Constraining the compensation state, structure and geophysical evolution of Sputnik basin on Pluto. In *Lunar and Planetary Science LII*, Abstract #2099. Lunar and Planetary Institute, Houston.

Nimmo, F., B. Giese, and R. T. Pappalardo (2003) Estimates of Europa's ice shell thickness from elastically-supported topography. *Geophys. Res. Lett., 30*, doi:10.1029/2002GL016660.

Nimmo, F. (2004) What is the Young's modulus of ice? In Workshop on Europa's Icy Shell, Abstract #7005. Lunar and Planetary Institute, Houston.

Nimmo F. and Matsuyama I. (2007) Reorientation of icy satellites by impact basins. *Geophys. Res. Lett.*, *34*, L19203.

Nimmo F., Hamilton D. P., McKinnon W. B., et al. (2016) Reorientation of Sputnik Planitia implies a subsurface ocean on Pluto. *Nature*, *540*, 94-96.

O'Hara, S. T., and A. J. Dombard (2021) Downhill sledding at 40 AU: Mobilizing Pluto's chaotic mountain blocks. *Icarus, 356*, 113829.

Petrenko, V. F., and R. W. Whitworth (1999) Physics of Ice, Oxford Univ. Press, New York.

Potter, R. W. K., D. A. Kring, G. S. Collins, W. S. Kiefer, and P. J. McGovern (2012) Estimating transient crater size using the crustal annular bulge: Insights from numerical modeling of lunar basin-scale impacts, *Geophys. Res. Lett.*, *39*, doi:10.1029/2012GL052981.

Potter, R. W. K., D. A. Kring, G. S. Collins, W. S. Kiefer, and P. J. McGovern (2013) Numerical modeling of the formation and structure of the Orientale impact basin, *J. Geophys. Res. Planets*, *118*, 963-979.

Reuter D. C., Stern S. A., Scherrer, J., et al. (2008) Ralph: A Visible/Infrared Imager for the New Horizons Pluto/Kuiper Belt Mission. *Space Science Reviews*, *140***,** 129-154.

Rubin A. M. (1995) Propagation of Magma-Filled Cracks. *Annu. Rev. Earth Planet. Sci.*, *23*, 287-336.

Rubincam D. P. (2003) Polar wander on Triton and Pluto due to volatile migration. *Icarus*, *163*, 469-478.

Schenk P. M., Beyer R. A., McKinnon W. B., et al. (2018) Basins, fractures and volcanoes: Global cartography and topography of Pluto from New Horizons. *Icarus*, *314*, 400-433.

Simpson, R. W. (1997) Quantifying Anderson's fault types, *J. Geophys. Res., 102*, 17,909-17,919.

Singer K. N., White O. L., Schenk P. M., et al. (2016) Pluto's putative cryovolcanic constructs. In *Lunar and Planetary Science XLVII*, Abstract #2276. Lunar and Planetary Institute, Houston.

Solomon S. C., and J. W. Head (1979) Vertical movement in mare basins: Relation to mare emplacement, basin tectonics, and lunar thermal history, *J. Geophys. Res., 84*, 1667-1682.

Spudis P. D. (1993) *The Geology of Multi-Ring Impact Basins*. 281 pp. Cambridge University Press.

Stern S. A., Bagenal F., Ennico K., et al. (2015) The Pluto system: Initial results from its exploration by *New Horizons*. *Science*, *350*, aad1815.

Stern S. A., White O. L., McGovern P. J., et al. (2021) Pluto's Far Side. *Icarus*, *356*, 113805.

Trowbridge A. J., Melosh H. J., Steckloff J. K., and Freed A. M. (2016) Vigorous convection as the explanation for Pluto's polygonal terrain. *Nature*, *534*, 79-81.

Turcotte D. L., Willemann R. J., Haxby W. F., Norberry J. (1981) Role of membrane stresses in the support of planetary topography. *J. Geophys. Res. Solid Earth, 86*, 3951-3959.

Umurhan O. M., Howard A. D., Moore J. M., et al. (2017) Modeling glacial flow on and onto Pluto's Sputnik Planitia. *Icarus*, *287*, 301-319.

Vaughan, D. G. (1995). Tidal flexure at ice shell margins. *J.Geophys. Res., 100*, 6213–6224.

Wessel, P., (1993), Observational Constraints on Models of the Hawaiian Hot Spot Swell. *J. Geophys. Res., 98*, 16-095-16,104.

Wei, Q. et al., Young Surface of Pluto's Sputnik Planitia Caused by Viscous Relaxation, Astrophys. Journ. Lett. 856 (2018), L14, doi.org/10.3847/2041-8213/aab54f

White, O. L., et al. (2017), Geological mapping of Sputnik Planitia on Pluto. *Icarus, 287*, 261-286.

Table 1: Nominal Model Parameters.

Parameter	*Value*	*Source*
Ice shell density ρ_{ice}	920 kg/m^3	Nimmo et al., 2016
Ice shell Young's Modulus E	5x10^9 Pa	See Section 4
Ocean density ρ_{ocean}	1000 kg/m^3	Nimmo et al., 2016
Acceleration of gravity *g*	-0.62 m/s^2	Stern et al. 2015
Ice shell Poisson's Ratio ν	0.3	Nimmo et al., 2016
Nitrogen ice infill density ρ_{fill}	1000 kg/m^3	Nimmo et al., 2016
Ice shell angle of internal friction ϕ	30°	
Ice shell cohesion *c*	1x10^6 Pa	

Table 1. Material properties adopted for the FEM models.